

High-mass X-ray binaries in nearby metal-poor galaxies: on the contribution to nebular He II emission

Peter Senchyna^{1*}, Daniel P. Stark¹, Jordan Mirocha^{2,3}, Amy E. Reines⁴, Stéphane Charlot⁵, Tucker Jones^{6,7}, and John S. Mulchaey⁸

¹ Steward Observatory, University of Arizona, 933 N Cherry Ave, Tucson, AZ 85721 USA

² Department of Physics and McGill Space Institute, McGill University, 3550 rue University, Montreal, QC, H3A 2T8, Canada

³ CITA National Fellow

⁴ eXtreme Gravity Institute, Department of Physics, Montana State University, Bozeman, MT 59717, USA

⁵ Sorbonne Université, CNRS, UMR7095, Institut d’Astrophysique de Paris, F-75014, Paris, France

⁶ Department of Physics, University of California Davis, 1 Shields Avenue, Davis, CA 95616, USA

⁷ Institute of Astronomy, University of Hawaii, 2680 Woodlawn Drive, Honolulu, HI 96822, USA

⁸ Observatories of the Carnegie Institution of Washington, 813 Santa Barbara Street, Pasadena, CA 91101, USA

Accepted XXX. Received YYY; in original form ZZZ

ABSTRACT

Despite significant progress both observationally and theoretically, the origin of high-ionization nebular He II emission in galaxies dominated by stellar photoionization remains unclear. Accretion-powered radiation from high-mass X-ray binaries (HMXBs) is still one of the leading proposed explanations for the missing He⁺-ionizing photons, but this scenario has yet to be conclusively tested. In this paper, we present nebular line predictions from a grid of photoionization models with input SEDs containing the joint contribution of both stellar atmospheres and a multi-color disk model for HMXBs. This grid demonstrates that HMXBs are inefficient producers of the photons necessary to power He II, and can only boost this line substantially in galaxies with HMXB populations large enough to power X-ray luminosities of 10^{42} erg/s per unit star formation rate (SFR). To test this, we assemble a sample of eleven low-redshift star-forming galaxies with high-quality constraints on both X-ray emission from *Chandra* and He II emission from deep optical spectra, including new observations with the MMT. These data reveal that the HMXB populations of these nearby systems are insufficient to account for the observed He II strengths, with typical X-ray luminosities or upper limits thereon of only 10^{40} – 10^{41} erg/s per SFR. This indicates that HMXBs are not the dominant source of He⁺ ionization in these metal-poor star-forming galaxies. We suggest that the solution may instead reside in revisions to stellar wind predictions, softer X-ray sources, or very hot products of binary evolution at low metallicity.

Key words: X-rays: galaxies – X-rays: binaries – galaxies: stellar content

1 INTRODUCTION

As the nearest collections of young and very metal-poor stars in the universe, local star-forming dwarf galaxies represent a crucial testbed for models of stellar populations at low metallicity. Nebular emission lines from highly-ionized gas provide a window onto the shape of the ionizing spectra of these systems in the extreme ultraviolet (EUV, 10–100 eV). The EUV potentially contains contributions from both the

hottest stars and emission from gas heated by compact object accretion and shocks, all of which are highly uncertain at very low-metallicity. The promise of obtaining quantitative constraints on these processes with deep spectroscopy is alluring, but physically interpreting this nebular emission has proved challenging.

In particular, the presence of nebular He II emission in nearby star-forming regions remains a puzzle three decades after it was first noted (Garnett et al. 1991, and references therein). The difficulty in understanding this emission is rooted in the very high energy of the photons necessary

* E-mail: senchp@email.arizona.edu

to doubly-ionize helium (> 54.4 eV, or > 4 Ryd) and thus power the recombination spectrum of He II; most notably, He II $\lambda 4686$ Å and $\lambda 1640$ Å. Theoretical stellar atmosphere models generally predict very little emergent flux beyond 54.4 eV, as He⁺ ionization in the atmosphere and expanding winds of massive stars introduces a strong absorption edge at this energy (e.g. Gabler et al. 1989; Pauldrach et al. 2001; Lanz & Hubeny 2003; Puls et al. 2005). In order to account for this apparent excess in flux at the He⁺-ionizing edge relative to the stellar models, Garnett et al. (1991) proposed two alternative non-stellar sources of ionizing radiation: radiative shocks and X-ray binaries.

Massive progress has since been made in expanding the sample of nebular He II detections both in the local Universe (e.g. Thuan & Izotov 2005; Kehrig et al. 2011; Shirazi & Brinchmann 2012; Kehrig et al. 2015; Senchyna et al. 2017; Kehrig et al. 2018; Berg et al. 2019b) and at $z \sim 1-4$ (e.g. Erb et al. 2010; Cassata et al. 2013; Berg et al. 2018; Nanayakkara et al. 2019). This body of observational evidence has made clear that nebular He II is strongly metallicity-dependent, and is likely ubiquitous among star-forming systems at metallicities $12 + \log \text{O}/\text{H} < 7.7$ (equivalently, $Z/Z_{\odot} < 0.1$; e.g. Senchyna & Stark 2019; Senchyna et al. 2019). Yet despite commensurate advances in stellar modeling, including state-of-the-art treatments of atmospheres, binarity, and rotation (e.g. Szécsi et al. 2015; Götberg et al. 2017; Eldridge et al. 2017; Götberg et al. 2018; Stanway & Eldridge 2019; Kubátová et al. 2019), there is as-yet no clear solution to the apparent modeling deficit of hard ionizing photons.

In recent years, the *Chandra* X-ray Observatory has revolutionized our understanding of X-ray binaries, enabling a reappraisal of their possible role in providing the missing ionizing photons. High-mass X-ray binaries (HMXBs), which power hard X-ray emission via accretion from a massive stellar companion onto a compact object (black hole or neutron star), have been shown to power nebular He II in cases where they act as the sole ionizing source in a nebula (Pakull & Angebault 1986; Kaaret et al. 2004b; Gutiérrez & Moon 2014). While it has long been established that HMXBs dominate the hard X-ray flux ($\gtrsim 1$ keV) of actively star-forming galaxies in the local Universe (e.g. Grimm et al. 2003; Mineo et al. 2012), early studies largely ignored very low-metallicity galaxies due to their faintness. Now, strong evidence has arisen that the X-ray luminosity per unit of star formation rate increases by nearly an order of magnitude in extremely metal-poor galaxies ($Z/Z_{\odot} \lesssim 0.1$) relative to those at near-solar metallicity (Mapelli et al. 2010; Prestwich et al. 2013; Basu-Zych et al. 2013; Brorby et al. 2014; Douma et al. 2015; Brorby et al. 2016; Brorby & Kaaret 2017). Theoretical models reproduce this general trend, suggesting that it is likely driven by the weaker stellar winds driven at low metallicity (e.g. Dray 2006; Linden et al. 2010; Fragos et al. 2013a). In particular, weaker winds lead to both more massive black holes and a higher incidence of HMXB systems undergoing Roche lobe overflow accretion, which both tend to produce more luminous X-ray binary populations.

The similarity of the metallicity dependence of HMXBs to that of nebular He II motivated Schaerer et al. (2019) to revisit the possibility that HMXBs may be solely responsible for this emission line in metal-poor star-forming galaxies. By assuming that the nebular He II in IZw18 NW is en-

tirely powered by the X-ray source observed in that cluster (c.f. Leboutteiller et al. 2017), Schaerer et al. (2019) derive a scaling relationship between He II flux and hard X-ray luminosity. Applying this to the population synthesis models of Fragos et al. (2013a,b), the authors demonstrate that the metallicity-dependent HMXB population produces a trend in the strength of He II relative to H β similar to that observed. Though suggestive, the model presented by Schaerer et al. (2019) has yet to clear two critical hurdles. First, it has yet to be demonstrated through full photoionization modeling that an HMXB spectrum can successfully power nebular He II when combined with stellar ionizing flux. Second, a detailed galaxy-by-galaxy investigation of both He II and X-ray constraints has not yet been conducted for more than a handful of systems (e.g. Thuan & Izotov 2005; Kehrig et al. 2018).

In this paper, we will test the hypothesis that HMXBs dominate the production of He II in star-forming galaxies from both a theoretical and observational perspective. First, we produce a grid of photoionization models with input SEDs reflecting the joint impact of young stellar populations and a variable HMXB contribution, and examine the impact of the latter on the predicted nebular line spectrum (Section 2). Then, leveraging recent work targeting metal-poor galaxies with both *Chandra* and high-resolution optical spectroscopy including data from Keck and new measurements from the MMT 6.5m telescope, we assemble a sample of eleven star-forming regions with robust constraints on both X-ray emission and nebular He II in Section 3. In Section 4 we examine these observational constraints in the context of the photoionization model results, providing a stringent empirical test of the claim that HMXBs dominate production of He⁺-ionizing photons in these systems. We conclude in Section 5.

2 MODELING GAS PHOTOIONIZED BY STARS AND HMXBS

In order to investigate the possibility that He II or other high-ionization emission lines are powered by high-mass X-ray binaries, we construct a semi-empirical framework to model this scenario explicitly. This requires us first to construct a model SED representing the combined ionizing spectrum of both massive stars and the emission from HMXB accretion disks. Then, we use a photoionization modeling framework to simulate the reprocessing of this ionizing spectrum through surrounding gas, producing predictions about the resultant nebular emission. We describe these two steps below in Section 2.1, then discuss the results and predictions of this modeling in Section 2.2.

2.1 Methodology

Our primary goal in this section is to assess the magnitude of the effect on nebular emission lines introduced by adding a HMXB spectrum to a stellar population model. While there are many existing prescriptions for full galaxy SED modeling in the literature (see e.g. Charlot & Longhetti 2001; Gutkin et al. 2016; Chevallard & Charlot 2016; Leja et al. 2017; Byler et al. 2017; Fioc & Rocca-Volmerange 2019), none yet account explicitly for the impact of HMXBs on nebular gas

emission. We describe our methodology in this subsection with comparison to other approaches in the literature where relevant.

2.1.1 Construction of the Spectral Energy Distribution

First, we describe how we construct the joint SED representing the ionizing flux emitted by massive stars and HMXBs. Since strong interstellar absorption precludes the direct observation of the EUV spectrum of massive stars or HMXBs, we must rely on models calibrated at higher or lower energies to predict the SED in this energy regime.

There are a variety of stellar population synthesis frameworks in the literature designed to predict the emergent flux from stars themselves (for a review, see [Conroy 2013](#)). As we will discuss further later in the paper, the shape of model stellar spectra in the EUV beyond the Lyman limit is highly uncertain, as these photons cannot be directly observed for any individual hot OB stars. In particular, the emergent flux from stars at and just beyond the He⁺-ionizing edge (54.4 eV, or 228 Å) is subject to substantial systematic uncertainties from both atmosphere and evolutionary models, and varies significantly between different population synthesis prescriptions. For instance, mass transfer can strip the donor star of its outer hydrogen layers, and potentially spin-up the accretor star sufficiently to change its evolution, both of which can enhance the escape rate for He⁺-ionizing photons which are easily blocked by the outer layers or dense winds of ‘typical’ massive stars (e.g. [Eldridge & Stanway 2012](#); [Szécsi et al. 2015](#); [Götberg et al. 2018](#); [Stanway & Eldridge 2019](#); [Götberg et al. 2019](#)). Accounting for high ZAMS rotation rates can also boost stellar flux in the EUV (e.g. [Maeder & Meynet 2000](#); [Vázquez et al. 2007](#); [Levesque et al. 2012](#); [Byler et al. 2017](#)). Significant uncertainties remain in the specific treatment of all of these factors, and they have not yet been considered simultaneously in a full population synthesis prescription.

For the purposes of this paper, we are primarily interested in constraining the potential impact of HMXBs on nebular emission when added to a stellar population. Thus, we focus solely on the latest version of the BPASS models accounting for binary evolutionary effects (2.2, described in [Stanway & Eldridge 2018](#)). These models incorporate prescriptions for some binary mass transfer processes which can have a substantial impact on emergent hard ionizing flux. It is important to note that modifications to our treatment of the stellar population that tend to increase the stellar contribution to flux at the He⁺-ionizing edge will decrease the relative impact of the HMXB spectrum. The BPASS flux predictions in the EUV are fairly representative of the state-of-the-art population synthesis codes, and in particular are lower than the newest results from the modified [Bruzual & Charlot \(2003\)](#) models ([Charlot & Bruzual](#), in prep.) incorporating newer theoretical stellar atmospheres for massive main-sequence and Wolf-Rayet stars (see [Stanway & Eldridge 2019](#); [Plat et al. 2019](#)).

The ionizing flux of a purely-stellar SED depends strongly on the assumed IMF, star formation history, and stellar metallicity. Since we are interested primarily in the HMXB contribution, we will make reasonable assumptions about the IMF and star formation history while leaving metallicity as a free parameter. We assume the

fiducial BPASS IMF, which consists of a broken power-law with a [Salpeter \(1955\)](#) slope (-2.35) over the mass range $0.5\text{--}300 M_{\odot}$. Extreme IMFs can enhance the He⁺-ionizing flux achieved, though not sufficiently to alone explain the strongest He II emission observed ([Stanway & Eldridge 2019](#)). We assume a constant star formation history that has proceeded for sufficiently long for the SED to stabilize (100 Myr), noting that instead adopting younger ages or adding young bursts will act to enhance the relative flux beyond 54.4 eV per unit SFR by increasing the number of early O and Wolf-Rayet stars (e.g. [Shirazi & Brinchmann 2012](#); [Chisholm et al. 2019](#)). Adopting a more extreme IMF or a star formation history weighted to younger ages would both increase the amount of hard ionizing flux from the stellar population at fixed SFR and reduce the relative impact of the HMXB spectrum on nebular line emission. Our relatively conservative assumptions about the stellar population synthesis prescription, IMF, and star formation history are chosen to provide a reasonable first estimate of the effect on nebular lines of adding HMXBs to a stellar ionizing spectrum.

With the stellar model prescription, IMF, and star formation history fixed, the most important variable affecting the ionizing flux of the stars themselves is then the stellar metallicity. As the bulk metallicity of a stellar population is lowered, reduced opacities in the stellar interior and atmosphere lead to both hotter temperature evolution for massive main-sequence stars and dramatically weakened stellar winds. These factors both directly lead to harder ionizing spectra for individual metal-poor stars, and the reduced impact of stellar wind mass loss at low metallicity can result in rotational and binary evolutionary effects playing a more prominent role in producing very hot stars. Models of these evolutionary stages are still highly uncertain and are not uniformly included in population synthesis predictions (e.g. [Szécsi et al. 2015](#); [Stanway et al. 2016](#); [Götberg et al. 2019](#), and references therein). We allow the stellar metallicity to vary from $Z = 0.020$ (solar, Z_{\odot}) to $Z = 0.001$ ($Z/Z_{\odot} = 5\%$), the lowest metallicity provided by the BPASSv2.2 grids. We note that adopting lower stellar metallicities would harden the stellar spectrum and further increase the maximal nebular He II flux powered by the stars alone. However, this metallicity range encompasses the full range of gas-phase oxygen abundances in our observational sample (assuming solar α/Fe ; [Table 1](#)); and as already discussed, such lower metallicities would further diminish the relative impact of HMXBs to He II.

In contrast to the stellar ionizing spectrum which drops off at energies above 54.4 eV due to absorption in stellar winds, the spectra of high-mass X-ray binaries are dominated by extremely hot accretion disks and peak at hard X-ray energies in the 1–10 keV range ([Figure 1](#)). Their spectra can be approximated with a multi-color disk (MCD) model ([Mitsuda et al. 1984](#)), which produces a modified blackbody spectrum representing gas at a range of temperatures in the accretion disk. This model is parameterized by the mass of the accreting black hole M_{BH} and the maximum radius of the disk R_{max} (in this work, we compute this spectrum using code from the ARES package¹; [Mirocha 2014](#)). For

¹ <https://bitbucket.org/mirochaj/ares>

black hole masses in the range of 10–100 M_{\odot} and radii of 10^3 – 10^5 cm, 54.4 eV remains solidly in the Rayleigh-Jeans tail of this spectrum, with flux far lower than at the SED peak in the keV range. Over this range, the black hole mass has the largest impact on flux at 54.4 eV for a fixed total luminosity, with more massive black holes yielding a softer spectrum and more flux at 54.4 eV. Increasing R_{\max} from 10^3 to 10^4 cm increases the flux at 54.4 eV by $\lesssim 25\%$ for black hole masses in this range, and essentially no change is seen when R_{\max} is increased further to 10^5 cm. Accordingly, we fix $R_{\max} = 10^4$ cm for our grid. HMXBs are known to undergo spectral transitions, though generally their spectrum is found to harden relative to an MCD spectrum likely due to Compton up-scattering during a super-Eddington accretion event (e.g. Kaaret & Feng 2013; Brorby et al. 2015), decreasing the flux at low ($\ll 1$ keV) energies. A more sophisticated model including Comptonization would thus cause the HMXB spectrum to be less efficient at producing photons at the He⁺-ionizing edge. For simplicity in this analysis, we adopt a single MCD model to represent the HMXB contribution to the total SED. While in massive galaxies we expect the X-ray spectrum to be a composite of several active HMXBs, the total unresolved X-ray luminosity of most nearby dwarf galaxies studied in Brorby et al. (2014, 2016, 2018) is actually suggestive of the luminosity of individual HMXBs resolved in larger spiral galaxies (e.g. Mineo et al. 2012), so this assumption may actually be more appropriate for the study of He II in the lowest-metallicity, lowest-mass galaxies found locally.

We are interested in the impact of explicitly varying the HMXB contribution on high-ionization nebular emission. Thus, we incorporate as an additional parameter the X-ray luminosity measured in a broad *Chandra* band (erg/s) produced per unit of star formation (M_{\odot}/yr), hereafter referred to as the X-ray production efficiency: $L_{X,0.5-8\text{keV}}/\text{SFR}$. Previous observations with *Chandra* provide guidance as to the range of values of this parameter attained in local galaxies. For the purposes of this study, we allow this quantity to vary over a broad range bracketing the values typically measured in nearby dwarf galaxies (e.g. Brorby et al. 2016) by several orders of magnitude: 10^{40} – 10^{44} erg/s/ (M_{\odot}/yr) .

Figure 1 compares these two SED components for a representative model in our grid. We plot here a BPASS model computed with the above assumptions (constant star formation history at 1 M_{\odot}/yr and fiducial IMF) at $Z = 0.004$ ($Z/Z_{\odot} = 0.2$). Next to this, we plot an MCD spectrum assuming $R_{\max} = 10^4$ cm for $M_{\text{BH}} = 10$ –100 M_{\odot} , in each case normalized in the 0.5–8 keV band to the median X-ray production efficiency in our grid: 10^{42} erg/s/ (M_{\odot}/yr) . This particular X-ray production efficiency is chosen such that the HMXB spectrum begins to impact significantly on the total EUV flux. At this X-ray luminosity per unit of star formation, the Rayleigh-Jeans tail of the MCD spectrum approaches the stellar contribution to the SED at the He⁺-ionizing edge as the black hole mass is increased.

2.1.2 Photoionization Modeling

Accurately predicting the nebular emission powered by HMXBs requires photoionization modeling, taking into account the joint effects of both HMXBs and stars in heating and ionizing their surrounding gas. We use the code CLOUDY

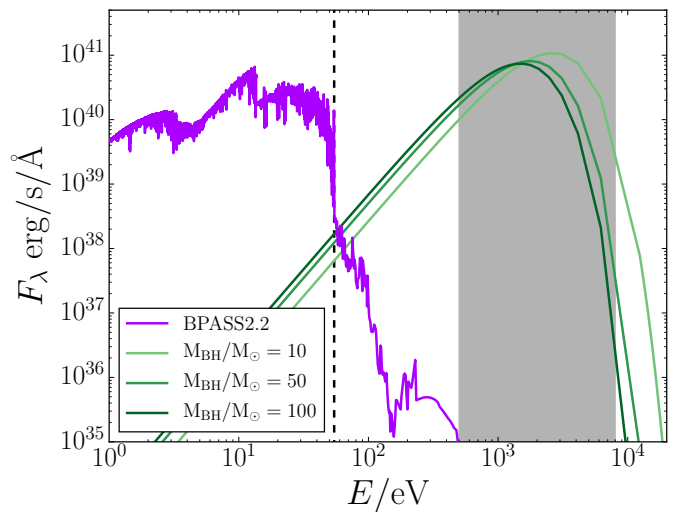


Figure 1. Representative SEDs for a model stellar population (BPASS v2.2, constant star formation at $1M_{\odot}/\text{yr}$, $Z = 0.004$) and a model HMXB (multi-color disk spectrum, $R_{\max} = 10^4$ cm, with $M_{\text{BH}}/M_{\odot} = 10$ –100). The HMXB spectrum is normalized in the 0.5–8 keV range (shaded grey) to the median X-ray production efficiency adopted in our grid: $L_{X,0.5-8\text{keV}}/\text{SFR} = 10^{42}$ erg/s/ (M_{\odot}/yr) . At this X-ray normalization, the Rayleigh-Jeans tail of the HMXB spectrum is within an order of magnitude of the stellar SED at the He⁺-ionizing edge (black dashed line).

(version 17.1, detailed in Ferland et al. 2017) to perform this part of the analysis. This photoionization code natively handles the processing of X-rays by nebular gas, including accounting for secondary ionizations. Following the standard methodology for modeling integrated light from star-forming galaxies (e.g. Byler et al. 2017), we assume a closed radiation-bounded spherical geometry consisting of a shell of material located sufficiently far from the central source (10^{19} cm) to be essentially plane-parallel. We allow the computation to iterate to convergence up to 5 times (typically only 3 are required), and stop the calculation once the temperature drops below 100 K or the edge of the hydrogen ionization front is reached (beyond either of which nebular line emission will be minimal). We run the CLOUDY models with a separate high-resolution input file for each SED, and measure the strength of the emission lines we are interested in directly from the saved output. To organize and analyze the grid, we utilize a modified version of the grid construction tools developed as part of CLOUDYFSPS (Byler 2018). Our approach is appropriate for our model of radiation-bounded H II regions surrounding recently-formed young stellar populations, but modeling more massive galaxies with several dominant generations of stars generally benefits from more complex approaches (e.g. Charlot & Longhetti 2001). Considering density-bounded model conditions is also beyond the scope of this paper, but Plat et al. (2019) demonstrate that the suppression of lower-ionization emission that these conditions introduce is generally inconsistent with the nebular properties of a broader sample of local He II-emitters.

There are several other important variables describing the gas to consider in this modeling scheme. We fix the gas density to $n_{\text{H}} = 10^2$ cm⁻² to approximate the typical values

measured from [S II] in nearby star-forming galaxies, including those which power strong high-ionization line emission (e.g. Brinchmann et al. 2008; Senchyna et al. 2017; Berg et al. 2019a). While typical H II region densities may be somewhat higher in galaxies in the early universe (e.g. Shirazi et al. 2014; Sanders et al. 2016), this is unlikely to significantly affect recombination lines such as He II (e.g. Plat et al. 2019). Since in this work we focus on metal-poor star-forming dwarf galaxies with low dust extinction measurements, we do not consider the effects of extinction or depletion onto dust in this analysis (though these effects are very important for general galaxy modeling; see e.g. Gutkin et al. 2016). The attenuation introduced by dust extinction is minimal for X-ray photons (dominated by small-angle forward scattering; Draine 2011) and we only consider observed optical line ratios after correction for extinction according to the Balmer decrement (Section 3).

Next, we must consider the gas-phase metallicity and chemical abundance patterns, which directly impact upon both metal line strengths and thereby the gas cooling efficiency and thus temperature. We fix the gas abundance patterns to those adopted by Dopita et al. (2000), which is based upon the solar abundances found by Anders & Grevesse (1989) with an additional empirically-motivated scaling of N/O with O/H imposed to account for the secondary production of nitrogen. In this first analysis, we scale the gas-phase metal abundances directly with the metallicity Z of the stellar population, while noting that allowing for an offset in this ratio could enhance the contribution of stellar ionizing flux to the production of high-ionization metal lines (e.g. Steidel et al. 2016; Senchyna et al. 2019).

Finally, we also allow the gas ionization parameter U to vary. This dimensionless quantity parametrizes the relative density of hydrogen-ionizing photons to the gas density:

$$U = \frac{Q_{\text{H}}}{4\pi R^2 n_{\text{H}} c}, \quad (1)$$

where Q_{H} is the total number of hydrogen-ionizing photons emitted by the source spectrum per second, c is the speed of light, and R is the radius of the ionized region. In this effectively plane-parallel case, the Strömgren sphere radius is approximately equal to the inner radius of the shell, and their distinction is unimportant (e.g. Charlot & Longhetti 2001; Byler et al. 2017). Nebular line ratios are typically insensitive to changes in R and Q_{H} that preserve $\log U$ (e.g. Evans & Dopita 1985; McCall et al. 1985). Since we fix the radius, specifying the ionization parameter implicitly normalizes the input spectrum. We allow this parameter to vary between $-3 < \log U < -1$, which spans the range typically observed in galaxies dominated by recent star formation.

2.2 Modeling Results and Predictions

The framework described above results in a model for a composite stellar and HMXB spectrum with four free parameters. These are metallicity Z (of both the stars and the gas, which we couple); the ionization parameter of the gas $\log U$; the X-ray production efficiency, $L_{\text{X},0.5-8\text{keV}}/\text{SFR}$; and the black hole mass for our MCD model, M_{BH} . We construct a grid of models while varying these parameters, and extract the CLOUDY predicted line fluxes for each point therein, al-

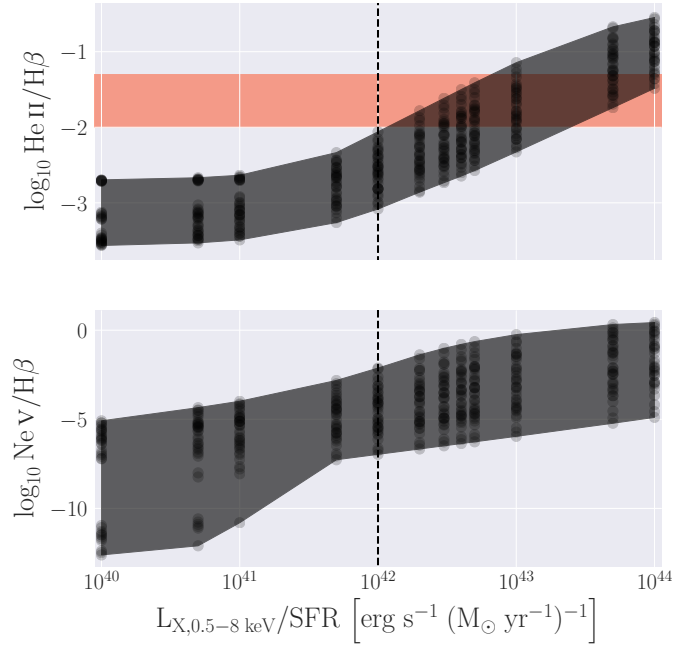


Figure 2. Line fluxes for He II $\lambda 4686$ and Ne V $\lambda 3426$ (top and bottom panels, respectively) relative to H β for all points in our model grid, plotted as a function of the X-ray luminosity per unit of star formation. The individual photoionization model grid points are displayed as black circles, and we outline in grey the flux range spanned by the models at each value of $L_{\text{X},0.5-8\text{keV}}/\text{SFR}$. In the top panel for He II, we shade in red the range of values observed for this line in low-metallicity nearby star-forming galaxies (e.g. Shirazi & Brinchmann 2012; Senchyna et al. 2017, 2019). He II is only boosted into the observed range of values for this line by the addition of the HMXB spectrum for systems with very high X-ray production efficiencies ($L_{\text{X},0.5-8\text{keV}}/\text{SFR} > 10^{42} \text{ erg s}^{-1}/(\text{M}_{\odot} \text{ yr}^{-1})$), marked by a vertical black dashed line).

lowing us to investigate the relative impact of these variables on nebular line emission.

We are particularly interested in how varying the HMXB contribution to the spectrum impacts the high-ionization nebular lines. In Figure 2, we plot the predicted line fluxes for He II $\lambda 4686$ and Ne V $\lambda 3426$ relative to H β for our entire grid as a function of the X-ray production efficiency. These two species have ionization potentials of 54 eV and 97 eV (respectively). As the X-ray production efficiency is increased from 10^{40} – 10^{44} erg/s at a star formation rate of $1 \text{ M}_{\odot}/\text{year}$, we find that the range of flux in He II relative to H β is increased by 2 orders of magnitude. The effect on Ne V is even more dramatic, increasing from essentially unobservable at $< 10^{-5}$ times the flux of H β to uniformly greater than this limit for the highest X-ray production rates. At the highest X-ray luminosities per SFR tested, both lines approach the flux of H β , indicating that the composite spectrum is effectively dominated by the hard Rayleigh-Jeans tail of the HMXB model. If we assume HMXBs provide the photons necessary to power He II and Ne V, then our models suggest we should observe a trend between enhanced flux in these lines relative to H β and the X-ray production efficiency.

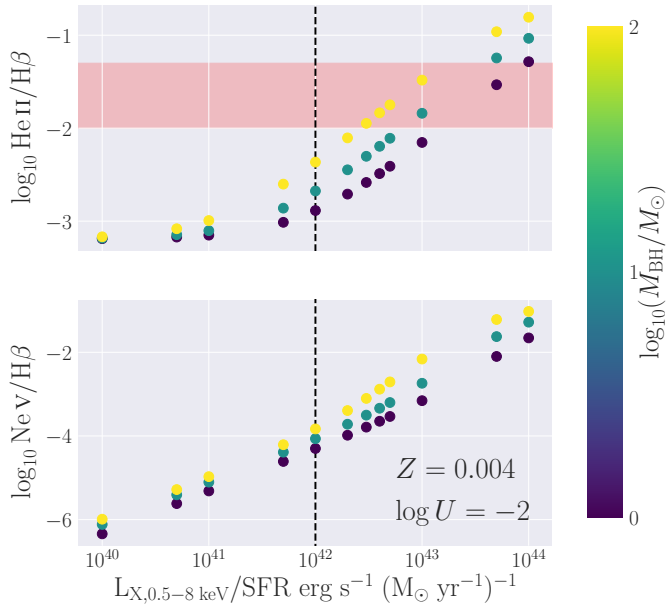


Figure 3. Same as Figure 2, but displaying a subset of the models with metallicity and ionization parameter fixed to $Z = 0.004$ and $\log U = -2$ to illustrate the dependence of the nebular lines on M_{BH} . Increasing the black hole mass from 1–100 M_{\odot} can effectively boost the prominence of He II by up to nearly an order of magnitude, but this only has a modest effect at low $L_{\text{X},0.5-8\text{keV}}/\text{SFR}$ values where the stellar spectrum dominates the EUV.

However, He II and Ne V are only substantially affected by the HMXB spectrum for systems with very large X-ray output relative to their star formation rate. As the X-ray production efficiency is increased from 10^{40} to 10^{41} erg/s per unit SFR, the ratio of He II $\lambda 4686/\text{H}\beta$ remains in the range observed for the BPASSv2.2 models alone, with the maximum achieved value increasing only from He II/H β = 0.20% to 0.23%. This is an order of magnitude below measurements in metal-poor dwarf galaxies, which span 1–5% (the red band in Figure 2, e.g. Shirazi & Brinchmann 2012; Senchyna et al. 2019). None of the models exceed 1% flux in He II or Ne V relative to H β until $L_{\text{X},0.5-8\text{keV}}/\text{SFR}$ exceeds 10^{42} erg s $^{-1}$ at 1 M_{\odot} yr $^{-1}$ (marked with a dashed black line in Figure 2). That is, galaxies with HMXB populations less luminous per SFR than this cutoff do not produce sufficient flux in the EUV to power He II at the level observed locally.

Though both He II and Ne V increase in strength relative to H β as the X-ray production efficiency is increased, the dispersion in their flux at fixed $L_{\text{X},0.5-8\text{keV}}/\text{SFR}$ evident in Figure 2 illustrates that they are also sensitive to the other model parameters (M_{BH} , $\log U$, and Z). We now investigate the impact of these variables in-turn, starting with the model black hole mass. In Figure 3, we fix the metallicity and ionization parameter to $Z = 0.004$ and $\log U = -2$ while allowing M_{BH} to vary over our full grid range (1–100 M_{\odot}). At X-ray production efficiencies below 10^{42} erg/s at 1 M_{\odot} /year, the modeled black hole mass has essentially no effect, since the EUV is still largely dominated by the stellar SED. At higher values of $L_{\text{X},0.5-8\text{keV}}/\text{SFR}$ where the HMXB spectrum begins to impact significantly on the EUV, we see

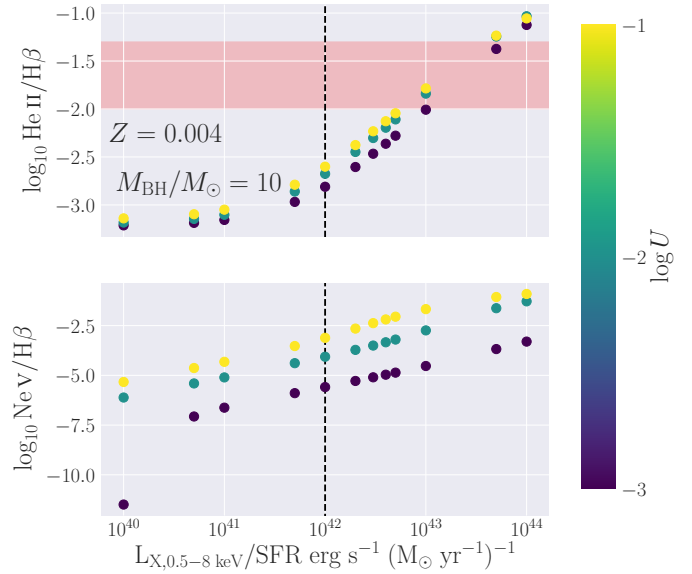


Figure 4. Same as Figure 2, but with metallicity and black hole mass fixed to $Z = 0.004$ and $M_{\text{BH}}/M_{\odot} = 10$ to investigate the dependence of the various lines on $\log U$. The relative strength of Ne V to H β is strongly dependent on $\log U$, increasing with this quantity by up to more than five orders of magnitude with other parameters fixed. However, He II is only modestly affected by an increase in the ionization parameter (especially at low $L_{\text{X},0.5-8\text{keV}}$), due to the fact that both He II and H β are re-combination lines.

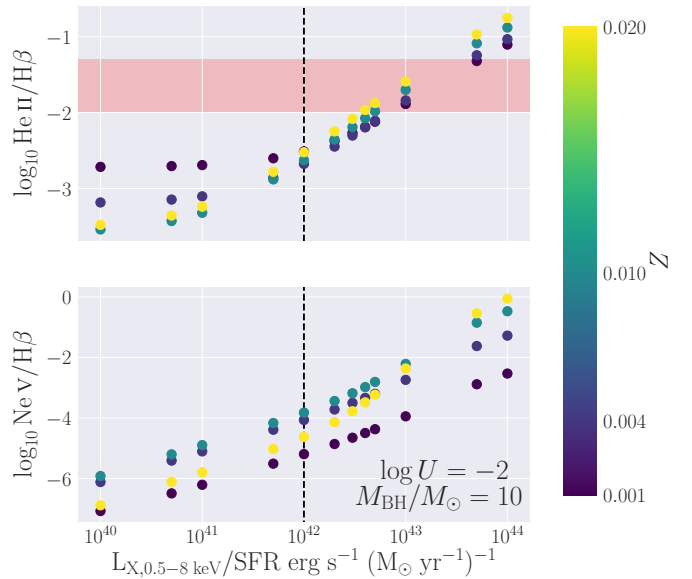


Figure 5. Same as Figure 2, but with the ionization parameter and black hole mass fixed to $\log U = -2$ and $M_{\text{BH}}/M_{\odot} = 10$, while the metallicity Z is allowed to vary. At low X-ray production efficiencies where the stellar SED dominates (left of the dashed line), He II is substantially more affected by decreasing metallicity than by $\log U$ or M_{BH} , increasing by nearly an order of magnitude as the metallicity is decreased. Ne V shows a more complicated behavior, due to the competing effects of increased gas temperature and diminishing neon abundances with decreasing metallicity.

that increasing the black hole mass boosts both Ne v and especially He II (since it is produced at lower energies). This is because a higher black hole mass yields a softer MCD spectrum (Figure 1), allowing the HMXB flux to play a larger role in the ionization structure of the nebula.

The gas geometry can also significantly affect the prominence of He II and Ne v with the input spectrum fixed (Figure 4). Increasing $\log U$ from -3 to -1 can increase Ne v/H β by nearly 3 orders of magnitude, by effectively expanding the size of the highest-ionization part of the H II region. However, $\log U$ has a smaller effect on the flux of He II relative to H β ($\lesssim 0.2$ dex). Since He II and H β are recombination lines, their ratio is fixed to first-order by the hardness of the input ionizing spectrum (e.g. Hummer & Storey 1987; Draine 2011; Senchyna et al. 2017).

The metallicity also plays a role in modulating the strength of He II and Ne v. In the regime where the stellar SED dominates He II production (left of the dashed line in Figure 5), He II is most strongly affected by metallicity, increasing by nearly an order of magnitude as metallicity drops from $Z = 0.02$ to 0.001 . As mentioned in Section 2.1, this is due to the hardening of the stellar SED with decreasing metallicity. At high X-ray production efficiencies (right of the dashed line), He II/H β decreases modestly with decreasing metallicity, due to the lowering of the recombination rate with increasing gas temperature (Hummer & Storey 1987). In contrast, Ne v/H β displays a very different behavior; at all but the highest X-ray production efficiencies, Ne v/H β peaks at $Z = 0.01$ before dropping at lower metallicity. Since the adopted stellar SED is too soft to contribute effectively to these lines, this behavior is due primarily to gas physics, with a competition between the diminishing abundance of neon and the increasing electron temperature (due to less efficient cooling). At the lowest metallicities ($Z < 0.01$), the diminishing neon abundance dominates, and Ne v become less prominent with decreasing metallicity. At the highest X-ray production efficiencies, gas heating is far more efficient, and this line simply decreases in strength with decreasing abundance over the entire metallicity range.

While M_{BH} , $\log U$, and Z all impact on He II and Ne v to some degree, our full set of photoionization models suggest two testable observational predictions independent of these variables if we assume that HMXBs dominate He II production. First, strong He II emission should be associated with very high X-ray production efficiencies: that is, X-ray luminosities in-excess of 10^{42} erg/s for a galaxy forming stars at $1 M_{\odot}$ /year. And second, stronger He II relative to H β (and, with greater dispersion due to gas physics, Ne v/H β) should positively correlate with higher X-ray luminosities per unit star formation rate. In the remainder of this paper, we will test whether these predictions hold in a sample of local star-forming galaxies with both high-quality *Chandra* and optical line constraints.

3 OBSERVATIONS

Through photoionization modeling, we have established an observational test of the scenario in which HMXBs dominate the production of He II in star-forming galaxies (Section 2). To investigate this, we have collated archival *Chandra* ACIS-S imaging of nearby $z < 0.2$ star-forming dwarf galaxies and

assembled both ESI and new MMT spectra covering He II $\lambda 4686$ and (in several cases) Ne v $\lambda 3426$. Though X-ray detections have previously been published for several of the targets in our sample, the absence of reported coordinates for these X-ray sources and the fact that several of our collected datasets are unpublished requires that we reanalyze these X-ray data. We present the sample in Sections 3.1 and 3.2; the optical spectroscopy in Section 3.3; the *Chandra* data in Section 3.4; and describe the results of this joint optical and X-ray analysis in Section 3.5.

3.1 Selection of the Sample

In order to test whether HMXBs are responsible for He II, we need an observational sample with high-quality constraints on both X-ray emission and nebular He II. In particular, the X-ray imaging must have sufficiently high spatial resolution ($\lesssim 1''$) to confidently associate X-ray point sources with the spectroscopic targets, which is presently only attained by *Chandra*. In addition, the optical spectra must have sufficiently high spectral resolution and signal-to-noise to confidently deblend the narrow (< 500 km/s) nebular He II $\lambda 4686$ recombination line from the broad (> 1000 km/s) component originating in the winds of WR or very massive O stars, which is generally not possible with SDSS spectra (see e.g. Senchyna et al. 2017). In the past several years, we have acquired high resolution optical spectra for a total of eleven star-forming dwarf galaxies which have *Chandra* X-ray imaging observations available in the archive (Table 1). Though selected in different ways initially, all are actively star-forming galaxies at subsolar metallicity and thus potential hosts for metal-poor HMXB populations.

Eight of these eleven are galaxies targeted with *HST*/COS ultraviolet spectroscopy in Senchyna et al. (2017) and Senchyna et al. (2019) for which we also obtained deep echellette optical spectra (we will subsequently refer to these papers as S17 and S19, respectively). These galaxies were originally selected on the basis of either a detection of optical He II emission in an SDSS spectrum (S17) and as having gas-phase metallicity measurements placing them in the regime of extremely metal-poor galaxies (XMPs, $12 + \log \text{O}/\text{H} < 7.7$, $Z/Z_{\odot} \lesssim 0.1$; S19). All are compact regions of active star formation dominated by the light from young (typically < 50 Myr) stellar populations. We cross-matched the entire sample of sixteen presented in these publications with publicly-available observations in the *Chandra* Observation Catalog accessed via ChaSeR to obtain the subsample of eight with *Chandra* coverage discussed here². We refer the reader to these previous papers for a more thorough discussion of the sample properties.

We also obtained new deep optical spectra for three additional galaxies previously studied with *Chandra*. In particular, we targeted three galaxies classified as Lyman Break Analogues (LBAs; Heckman et al. 2005) and studied in X-rays using *Chandra* by Basu-Zych et al. (2013) and Brobry et al. (2016, hereafter B16) with the MMT Blue Channel spectrograph: SHOC042, J2251+1427, and SHOC595. These

² Note that while SB198 from S17 falls within the standard $10'$ search radius employed by ChaSeR, the optical target falls outside the footprint of the ACIS-S3 chip.

spectra provide coverage of both He II $\lambda 4686$ and Ne V $\lambda 3426$. We will discuss the reduction and analysis of these observations in Section 3.3 below.

3.2 Star Formation Rates and General Characterization

Before advancing to the high-quality optical spectra and *Chandra* data available for the galaxies in our sample, we will first discuss their bulk properties. All but one of the targeted systems (HS1442+4250) has an SDSS spectrum available as of the latest data release (DR15; Aguado et al. 2019), and the other (HS1442+4250) has an MMT spectrum described in S19. We derive distance estimates by comparing the redshifts measured in these spectra to the local flow model presented by Tonry et al. (2000) with $H_0 = 70$ km/s/Mpc, with this simply reverting to the cosmological distances for the most distant objects. We present these distances in Table 1, along with gas-phase metallicities and the references to their derivation.

Since the higher-resolution spectra discussed in Section 3.3 do not all provide access to both H β and H α , we obtain uniformly-calibrated measurements of the strong optical lines from the SDSS spectra for reddening correction and SFR estimation. We follow the procedure outlined in S17; S19: in particular, we measure line fluxes using a custom PYTHON routine based on MCMC fits (Foreman-Mackey et al. 2013) with a linear continuum plus Gaussian line model, and correct for extinction by comparing the observed Balmer decrement to that predicted from our direct determination of T_e with PYNEB (Luridiana et al. 2015), assuming an SMC extinction curve (Gordon et al. 2003) after correction for Galactic extinction (Schlafly & Finkbeiner 2011; Fitzpatrick 1999). We follow the procedure described in S17 using PYNEB to derive direct temperature metallicities (with [O III] $\lambda 4363$) for the three LBAs from the B16 sample, yielding uniform metallicity measurements for the entire sample (Table 1). In the case of HS1442+4250, we use an MMT Blue Channel spectrum obtained with the 300 lines/mm grating on January 25, 2017 (described in S19). To correct for aperture differences between this MMT spectrum and the other SDSS spectra, we derive an effective aperture correction by comparing the measured fluxes of the strong lines of H and O in MMT spectra taken in the same configuration and on the same night for SBSG1129+576 and J1119+5130 to their SDSS spectra. This yields consistent correction factors of 0.58 and 0.57 for SBSG1129+576 and J1119+5130 with a scatter of $\sim 3\%$ among the different lines, respectively; we adopt a value of 0.57 and add an additional statistical uncertainty of 10% in this conversion.

These measurements of H α and H β provide a direct estimate of the current star formation rate in the spectral aperture where He II is constrained. Following the standard methodology, we convert the dust-corrected Balmer line luminosities into SFR estimates using a conversion factor derived from the same BPASS v2.2 models employed in the photoionization modeling (Section 2). In particular, we assume $Z = 0.003$ (corresponding to the mean metallicity of our sample, $12 + \log O/H = 7.9$, assuming solar abundances) and the fiducial BPASS IMF (Salpeter slope). For each galaxy, we derive an SFR conversion factor appropriate for the effective age of the dominant stellar population by

choosing the constant star formation rate model with predicted H β equivalent width closest to that observed. The uncertainty in the resulting estimates (Table 1) represents the statistical uncertainties in the flux measurement and determination of $Q(\text{Lyc})/L_{\text{H}\alpha}$. These estimates only account for star formation within the spectroscopic aperture, and thus represent lower limits to the total star formation rate of the target galaxies.

These bulk measurements reveal a diverse set of actively star-forming galaxies. They range in distance from ~ 10 to 800 Mpc, with all but the relatively distant LBAs from B16 residing at < 50 Mpc (redshifts $z \lesssim 0.01$). Their gas-phase metallicities span from the extremely metal-poor regime $12 + \log O/H = 7.5\text{--}7.7$ up to over half solar metallicity at $12 + \log O/H = 8.3$. Though they are all dominated by young stars, their absolute star formation rates span over four orders of magnitude, from $10^{-3.6}$ to $10^{0.77} M_{\odot}/\text{year}$.

3.3 Optical Spectroscopy

Here, we collate and summarize the deep optical spectral constraints available for the systems under study. As demonstrated in S17, nebular and broader stellar He II can be confused at the signal-to-noise and resolution typically attained in SDSS fiber spectra. We have specifically selected galaxies for which we have additional optical spectral constraints that can separate nebular from stellar He II and in some cases provide constraints on Ne V $\lambda 3426$, which probes even higher-energy photons. We obtained optical echelle spectra covering He II and H β (but not Ne V) for eight of the systems with the Echelle Spectrograph and Imager (ESI; Sheinis et al. 2002) on Keck II in 2016–2017 as part of an ongoing joint optical and ultraviolet spectroscopic campaign (S17; S19). We refer the reader to these previous publications for a detailed description of the Keck/ESI observations and analysis, and present the measurements of dust-corrected He II/H β derived from these spectra in Table 3.

We have also obtained several new spectra with the Blue Channel Spectrograph on the 6.5m MMT (MMT/BC) specifically targeting Ne V and He II (Table 2). We observed J2251+1327, SHOC595, and SHOC042 (LBAs from B16) on the night of September 10, 2018 with the 800 lines/mm grating and the $1.0'' \times 180''$ slit ($0.75 \text{ \AA}/\text{pixel}$ dispersion), at central wavelengths chosen to span the rest-wavelength range from Ne V $\lambda 3426$ to H β at the SDSS redshift of each target. The standard stars G24-9, Feige 110, and LB 227 (respectively) and a HeAr/Ne comparison lamp were observed either before or after each target object with the same spectrograph configuration for flux and wavelength calibration. In addition, on April 15 2018 we used the 300 lines/mm grating to observe an optical point-source identified in SDSS imaging as coincident with an X-ray source in the ACIS-S image of HS1442+4250 (see Section 4 for more details). All spectra were reduced using standard longslit techniques with a custom PYTHON pipeline.

To measure nebular He II confidently in these MMT/BC spectra, we follow the same technique adopted with the Keck/ESI data. In order to distinguish the nebular contribution from the broad > 500 km/s FWHM stellar component, we fit two Gaussians simultaneously to the He II $\lambda 4686$ line, with one constrained to narrow width comparable to that measured for the strong nebular lines (FWHM $< 7 \text{ \AA}$) and

Table 1. Basic properties of the eleven galaxies analyzed in this work, ordered by right ascension. Redshifts are measured from the strong optical lines in SDSS spectra (or, in the case of two of the XMPs, from an MMT spectrum; Senchyna et al. 2019), and the corresponding distances computed using the local velocity flow model presented by Tonry et al. (2000) as described in (Senchyna et al. 2017, 2019). We also present gas-phase metallicities measured using the direct- T_e method and star formation rates measured using the Balmer lines.

Name	RA (J2000)	Dec (J2000)	Sample	z	Distance (Mpc)	12 + log O/H (direct- T_e)	$W_{0,H\beta}$ (Å)	$\log_{10} \text{SFR}(H\beta)/(M_{\odot}/\text{yr})$
SHOC042	00:55:27.46	-00:21:48.7	B16	0.1674	805	8.21 ± 0.09	47 ± 4	0.77 ± 0.03
J0940+2935	09:40:12.87	+29:35:30.2	S19	0.0024	8	7.63 ± 0.14	37 ± 1	-3.58 ± 0.10
SB80	09:42:56.74	+09:28:16.2	S17	0.0109	46	8.24 ± 0.06	243 ± 17	-0.90 ± 0.02
SB2	09:44:01.87	-00:38:32.2	S17	0.0048	19	7.81 ± 0.07	274 ± 17	-1.61 ± 0.02
J1119+5130	11:19:34.37	+51:30:12.0	S19	0.0045	22	7.51 ± 0.07	50 ± 1	-2.31 ± 0.04
SBSG1129+576	11:32:02.64	+57:22:36.4	S19	0.0050	25	7.47 ± 0.06	81 ± 3	-2.45 ± 0.05
SB191	12:15:18.60	+20:38:26.7	S17	0.0028	10	8.30 ± 0.07	392 ± 23	-2.20 ± 0.02
SB111	12:30:48.60	+12:02:42.8	S17	0.0042	16	7.81 ± 0.08	102 ± 5	-2.37 ± 0.02
HS1442+4250	14:44:11.46	+42:37:35.6	S19	0.0023	11	7.65 ± 0.04	113 ± 4	-3.03 ± 0.05
J2251+1327	22:51:40.32	+13:27:13.4	B16	0.0621	279	8.29 ± 0.06	56 ± 1	0.22 ± 0.02
SHOC595	23:07:03.76	+01:13:11.2	B16	0.1258	589	8.07 ± 0.10	61 ± 4	0.49 ± 0.04

Table 2. A summary of the new MMT Blue Channel observations presented in this work.

Target	Airmass	Configuration Grating (slit)	Exposure (hours)
10 September 2018			
J2251+1327	1.2	800gpm (1.0" × 180")	2.3
SHOC595	1.3	800gpm (1.0" × 180")	1.6
SHOC042	1.4	800gpm (1.0" × 180")	1.6
15 April 2018			
HS1442+4250 X-ray source	1.1	300gpm (1.0" × 180")	0.17

the other forced to be broader than this cutoff. The results of these fits are displayed in Figure 6. We detect a distinct narrow component in J2251+1327 and SHOC042 at a relative strength of $\text{He II}/H\beta = 0.0070 \pm 0.0034$ and 0.0046 ± 0.0021 (respectively), and place a 3σ upper limit on the nebular component of $\text{He II}/H\beta < 0.0068$ for SHOC595. These relatively weak detections ($\text{He II}/H\beta < 0.01$) are consistent with the metallicities of these systems ($12 + \log \text{O}/\text{H} > 8.0$) in the context of the trend towards stronger He II at low metallicity (e.g. Figure 7 of Senchyna et al. 2019, which includes the other systems discussed in this paper). In addition, these MMT spectra place strong constraints on the presence of nebular $\text{Ne V } \lambda 3426$ ($\text{Ne V}/H\beta < 0.8$ in all three cases). These line measurements and dereddened 3σ upper limits where appropriate are reported in Table 3. We also include the measurement of $\text{Ne V}/H\beta = 0.79 \pm 0.36$ for SB111 (or J1230+1202) reported by Izotov et al. (2012). We discuss these measurements in the context of the *Chandra* constraints in the following section.

3.4 *Chandra* X-ray Imaging

All objects in our sample have publicly available *Chandra* ACIS-S imaging observations. While detections have been published for several of these systems in the past, these prior

studies generally do not include the coordinates of the identified X-ray sources and our sample also includes several galaxies covered by unpublished *Chandra* datasets. This requires that we reanalyze the *Chandra* data in a uniform way. We compare to these literature measurements where available in Appendix A. We first reprocessed the level 1 event files for these observations using the latest version of CIAO (4.11, CALDB version 4.8.2 Fruscione et al. 2006), focusing on the back-illuminated S3 chip which all targets were placed on. We used FLUXIMAGE to produce a clipped exposure map in the broad *Chandra* band, which we then used for source detection with a significance threshold of 10^{-6} run on the $\sqrt{2}$ series of pixel scales (see e.g. Mineo et al. 2012; Brorby et al. 2014).

The spatial resolution afforded by *Chandra* is a key advantage in conducting a study connecting X-ray observations to optical data. The astrometry of *Chandra* detections on the ACIS-S detector is accurate to $< 1.4''$ in 99% of cases in comparisons with ICRS optical counterparts³. Since we are concerned in this work with the potential impact of HMXBs on nebular line emission measured on spatial scales of $\sim 1''$ (Section 3.3), we are not interested in X-ray sources significantly offset from the optical galaxy. This is in contrast to much of the previous work on these galaxies, where significantly offset sources were included to account for the fact that HMXBs may be kicked up to hundreds of parsecs from their birthplace (e.g. Kaaret et al. 2004a; Zuo & Li 2010; Brorby et al. 2014). It is important to note that even with this resolution, we cannot unambiguously associate X-ray sources with the gas in which the observed He II is excited. At the distances of our targets, $1''$ corresponds to comoving physical distances of 50 pc to 3 kpc, larger than the sizes of individual star clusters in the local universe (e.g. Meurer et al. 1995).

We adopt the 99% confidence positional accuracy limit of $1.4''$ as a limiting radius to establish association between the X-ray sources and the observed optical line emission, and consider separations between $1.4''$ – $5''$ on an individual

³ CIAO manual: <http://cxc.cfa.harvard.edu/cal/ASPECT/celmon/>.

Table 3. Optical spectroscopic constraints on nebular He II and Ne V for our target galaxies (including 3σ upper limits where appropriate). All measurements have been dereddened using an SMC extinction curve and the Balmer decrement measured in the corresponding SDSS spectrum.

Name	He II $\lambda 4686/H\beta$ $\times 100$	Source (He II)	Ne V $\lambda 3426 / H\beta$ $\times 100$	Source (Ne V)
SHOC042	0.46 ± 0.21	MMT/BC (2018-09-10)	< 0.79	MMT/BC (2018-09-10)
J0940+2935	< 1.17	Keck/ESI (2017-02-21, S19)		
SB80	0.31 ± 0.03	Keck/ESI (2017-01-21, S17)		
SB2	1.30 ± 0.06	Keck/ESI (2017-01-20, S17)		
J1119+5130	2.64 ± 0.26	Keck/ESI (2017-02-21, S19)		
SBSG1129+576	< 0.42	Keck/ESI (2017-02-21, S19)		
SB191	< 0.14	Keck/ESI (2016-03-29, S17)		
SB111	3.94 ± 0.13	Keck/ESI (2017-01-20, S17)	0.79 ± 0.36	Izotov et al. (2012)
HS1442+4250	3.58 ± 0.06	Keck/ESI (2017-02-21, S19)		
J2251+1327	0.70 ± 0.34	MMT/BC (2018-09-10)	< 0.60	MMT/BC (2018-09-10)
SHOC595	< 0.68	MMT/BC (2018-09-10)	< 0.62	MMT/BC (2018-09-10)

basis (see Section 3.5 and Appendix A). To compute net count rates, fluxes, and 68% uncertainties for these detected sources in the 0.5–8.0 keV band, we ran SRCFLUX on the filtered level 2 event files assuming an absorbed power law model with photon index $\Gamma = 1.7$ and a neutral absorbing column with density N_H set to the Galactic value towards each system in the NRAO dataset of Dickey & Lockman (1990) accessed by COLDEN. This photon power law is a reasonable approximation of the shape of the assumed intrinsic MCD spectrum over the 0.3–8.0 keV band, and is commonly assumed in flux measurements for similar samples (e.g. Douna et al. 2015). Adopting a steeper index of $\Gamma = 2.0$ (corresponding to a softer spectrum, as in Mineo et al. 2012; Fabbiano 2006) would decrease the inferred fluxes by $12^{+1}_{-2}\%$. If no sources were detected within $1.4''$ from the SDSS ICRS coordinates on which the optical spectra were centered, we consider the target undetected in X-rays. In this case, we compute a 95% confidence upper limit to the count rate and flux using SRCFLUX. In both cases, we convert the observed fluxes to luminosities in the same band using the distance to each galaxy (Table 1). These measurements and upper limits are presented in Table 4.

One concern in computing the X-ray fluxes is the possibility that uncertainties in the absorbing column density of neutral gas towards each source might impact on the inferred X-ray luminosities. We do not have a robust way to estimate this internal absorption for these galaxies without X-ray spectral information or Ly α constraints (e.g. Thuan et al. 2004), so we follow the standard procedure for such data and correct only for Galactic N_H as described above. Fortunately, the galactic absorbing column density towards our sources is uniformly low ($N_H < 10^{21} \text{ cm}^{-2}$). Increasing the assumed value of N_H by a factor of five in the above-described SRCFLUX measurements increases the resulting $L_{X,0.5-8 \text{ keV}}$ values by a median factor of only 1.15, suggesting that the effect of accounting for additional absorption internal to the target galaxies would likely be small.

This procedure yields *Chandra* detections of seven of the galaxies in X-rays (Figure 7 and Table 4). We discuss the results in more detail in Section 3.5 and Appendix A.

3.5 Results

With both optical and X-ray data in-hand, we can now build a picture of the X-ray properties of the galaxies in our sample. For a detailed discussion of the results for each system, we refer the reader to Appendix A. Following the procedure described in Section 3.4, we detect X-ray emission cospatial with the star-forming clump targeted with optical spectroscopy in seven of the eleven galaxies in our sample (Table 4 and Figure 7). The resulting measurements of $L_{X,0.5-8 \text{ keV}}$ range over three orders of magnitude, with the nearest sources revealing X-ray luminosities of $1-40 \times 10^{38} \text{ erg/s}$ and the more distant LBAs residing at $2-7 \times 10^{41} \text{ erg/s}$. The available observations place strong upper limits on the X-ray luminosities of the undetected systems, constraining their luminosities to $\lesssim 10^{38} \text{ erg/s}$. We find good agreement with the X-ray luminosities measured by Brorby et al. (2014, 2016) for the subset of our *Chandra* observations previously analyzed in these works, but our more stringent matching of the X-ray and optical coordinates reveals two key differences with earlier analysis.

The undetected systems include two galaxies previously reported as HMXB hosts based upon the same *Chandra* data. For both SB111 and HS1442+4250 (Brorby et al. 2014), we identified a nearby X-ray source, but found that it resided at a distance of $11''$ and $8''$ (respectively) from the center of the star-forming region targeted with ESI (Figure 7). This offset is far larger than the uncertainty associated with the *Chandra* coordinates ($< 1.4''$ at 99% confidence). Even assuming the X-ray source resides at the same redshift, this places the object at a significant distance from the H II region in which we observe nebular He II (0.9 and 0.4 comoving kpc). In the case of SB111, the nearest X-ray source has no SDSS optical counterpart. However, the X-ray emission near HS1442+4250 is clearly associated with a faint $i = 21$ point source in the SDSS image (Figure 7). As detailed in Appendix A, we obtained an MMT/BC spectrum of this source and discovered broad emission lines consistent with Ly α and C IV at $z = 2.4$ (Figure 8). Thus, in this case the X-ray emission previously thought to belong to an ejected HMXB is actually associated with a background quasar. In both cases, we conclude the X-ray emission cannot be physically associated with the observed nebular He II.

Combined with the aperture SFR estimates from the

Table 4. Summary of the *Chandra* ACIS-S observations analyzed in this work. We highlight the program ID and PI and the observation time for each. The separation between the nearest detected X-ray source and the optical spectroscopic target is given in both arcseconds and comoving kpc. We provide the galactic column density N_{H} towards each source, and the count rate and derived luminosity if the target is detected with *Chandra* or the 95% confidence upper limits if not (see Section 3.4 and Appendix A).

Name	Chandra ObsID (PI)	Date	Exposure ks	r_{sep} arcsec (comoving kpc)	N_{H} 10^{20} cm^{-2}	Net count rate s^{-1}	$L_{\text{X},0.5-8\text{keV}}$ $10^{38} \text{ erg s}^{-1}$
SHOC042	16019 (Kaaret)	2014-01-31	22.7	0.2 (0.72)	2.67	0.00089 ± 0.00022	$6.55 \pm 1.61 \times 10^3$
J0940+2935	11301 (Prestwich)	2010-01-16	5.0	60.3 (2.34)	1.78	< 0.00054	< 0.34
SB80	19164 (Chandra)	2018-01-03	46.8	0.2 (0.05)	3.13	0.00015 ± 0.00007	4.94 ± 2.23
SB2	19463 (Mezcua)	2017-03-11	14.9	0.3 (0.03)	4.25	0.00078 ± 0.00033	4.00 ± 1.65
J1119+5130	11287 (Prestwich)	2009-11-07	11.7	2.2 (0.24)	1.16	0.00847 ± 0.00093	$38.97 \pm 4.29 (< 1.09) \dagger$
SBSG1129+576	11283 (Prestwich)	2010-07-06	14.8	0.8 (0.09)	1.00	0.00177 ± 0.00038	10.69 ± 2.28
SB191	7092 (Swartz)	2006-04-02	2.0	46.5 (2.25)	2.46	< 0.00137	< 1.33
SB111	11290 (Prestwich)	2010-07-26	12.0	11.1 (0.86)	2.54	< 0.00023	< 0.59
HS1442+4250	11296 (Prestwich)	2009-11-26	5.2	8.3 (0.44)	1.54	< 0.00053	< 0.62
J2251+1327	13013 (Basu-Zych)	2011-01-17	19.6	0.4 (0.53)	4.75	0.00216 ± 0.00037	$1.77 \pm 0.30 \times 10^3$
SHOC595	17418 (Kaaret)	2014-09-24	13.6	1.3 (3.59)	4.72	0.00076 ± 0.00026	$3.24 \pm 1.12 \times 10^3$

†The X-ray detection in this system is $> 2''$ away from the optical spectroscopic target and likely does not contribute to the observed He II, but is clearly associated with the galaxy; see Appendix A. We consider this galaxy detected for the purposes of this paper, but note the 95% confidence upper limit to the luminosity derived with SRCFLUX centered on the spectroscopic target and note this caveat in Figure 9 as well.

Balmer lines (Section 3.2), these *Chandra* detections provide a measurement of the X-ray production efficiency of these galaxies. These systems power luminosities $L_{\text{X},0.5-8\text{keV}}$ ranging from 4×10^{39} to 8×10^{41} erg/s at a fixed SFR of $1 \text{ M}_{\odot}/\text{year}$ (Appendix A). Crucially, none of the galaxies exceeds 10^{42} erg/s per $\text{M}_{\odot}/\text{year}$. We discuss the implications of these measurements in the context of our photoionization model predictions in the following section.

4 DISCUSSION

With the assembled set of eleven metal-poor galaxies with optical and X-ray constraints, we can test whether HMXBs are a plausible explanation for the observed nebular He II. In particular, we derived two key observational predictions from our photoionization modeling adopting the assumption that HMXBs provide the extra EUV ionizing radiation necessary to power He II (Section 2). First, we found that the HMXB spectrum could only boost the He II luminosity relative to $\text{H}\beta$ to $\gtrsim 1\%$ at extraordinarily large X-ray luminosities per star formation rate of $> 10^{42}$ erg/s at $1 \text{ M}_{\odot}/\text{year}$ (Figure 2). And second, our models indicate that this scenario should create a positive correlation between high X-ray luminosities at fixed SFR and strong high-ionization emission relative to $\text{H}\beta$ (especially high $\text{He II}/\text{H}\beta$).

First, we compare the X-ray production efficiencies attained by the galaxies in our sample to the results of our model grid. In Figure 9, we plot the flux ratio of He II to $\text{H}\beta$ as a function of the X-ray luminosity per unit star formation rate measured for these eleven galaxies, alongside our full set of photoionization models. Our targets with He II detections are entirely disjoint from the photoionization modeling, powering He II up to an order of magnitude stronger relative to $\text{H}\beta$ than expected. For instance, consider SB2, in which we detect He II at a high flux ratio with $\text{H}\beta$ of 0.0130 ± 0.0004 . This system is detected in X-rays as well, but at an X-ray

production efficiency of only $1.47 \pm 0.61 \times 10^{40}$ erg/s for a star formation rate of $1 \text{ M}_{\odot}/\text{year}$, two orders of magnitude lower than we estimate is required for the HMXB spectrum to reach the level of the stellar SED at the He^+ -ionizing edge. Seven of our target systems are detected in He II, including some of the highest values of $\text{He II}/\text{H}\beta$ yet measured locally (up to 0.04), and yet all are found to be relatively inefficient producers of X-ray flux. None reach an X-ray production efficiency of 10^{42} erg/s for a star formation rate of $1 \text{ M}_{\odot}/\text{year}$, which we predict is the minimum required for HMXBs to begin powering strong He II. This indicates that HMXBs (with a standard MCD spectrum) in these galaxies do not produce sufficient flux at the He^+ -ionizing edge to account for the observed He II emission.

Our photoionization models also make a clear prediction that if HMXBs are primarily responsible for He^+ -ionization, we should observe a correlation between $\text{He II}/\text{H}\beta$ and the SFR-normalized X-ray luminosity, with the strongest He II emission expected in galaxies most efficient in X-ray production. Our observational results show no evidence for a relationship between these features. In particular, the six galaxies with the strongest X-ray emission (exceeding 10^{41} erg/s in $L_{\text{X},0.5-8\text{keV}}$ for a SFR of $1 \text{ M}_{\odot}/\text{year}$) include only three He II detections, with all but one revealing relatively-weak He II ($\text{He II}/\text{H}\beta \lesssim 0.01$). The most prominent cases of He II emission in our sample ($\text{He II}/\text{H}\beta > 0.025$, among the highest observed in any star-forming galaxies) occur in three systems: J1119+5130, SB111, and HS1442+4250. The latter two of these are both confidently undetected in X-rays, with limiting X-ray production efficiencies as low as $< 1.2 \times 10^{40}$ erg/s at $1 \text{ M}_{\odot}/\text{year}$. In the third case (J1119+5130), it is highly unlikely that the X-ray emission associated with the galaxy is capable of powering the observed He II due to the sizable spatial offset from the spectroscopic aperture (Section 3.5). Analogously to He II, our models also suggest that the relative strength of Ne V should correlate with higher X-ray production efficiencies if it is also powered by HMXBs.

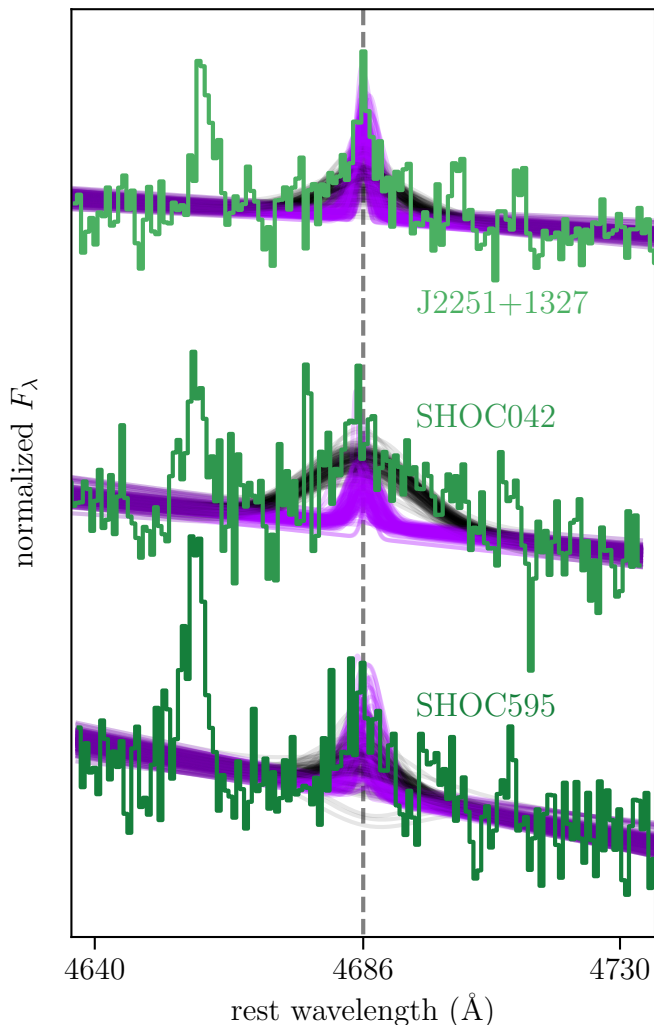


Figure 6. The He II $\lambda 4686$ complex for each of the LBAs observed with Blue Channel (green). We overplot models drawn from the fit posterior distribution, decomposed into the broad (black) and narrow (purple) components atop the fit linear continuum. A narrow component is detected at $> 2\sigma$ for J2251+1327 and SHOC042, whereas the profile for SHOC 595 appears to be completely dominated by a line profile with width significantly larger than the strong nebular lines.

While only three of our systems have Ne v constraints, none of these three reveal detections of both X-ray emission and Ne v. The X-ray output of these systems appears entirely decoupled from the strength of high-ionization emission, contrary to our expectations assuming the two are physically related.

A potential source of concern in this analysis is HMXB variability, which could plausibly cause scatter relative to the models in Figure 9 if systems were observed with optical spectroscopy during an outburst and in X-rays during a period of quiescence. Due to their nature as accretion-driven systems, HMXBs exhibit variability in both spectral shape and normalization during outbursts (e.g. Mineo et al. 2012; Kaaret & Feng 2013; Brorby et al. 2015). We see tentative possible evidence for variability in the X-rays in the multiple

observations of SB80 and SHOC595 (Section 3.5). However, the strongest nebular He II emission in our sample (in SB111) was found at nearly identical strength relative to H β in our 2017 Keck/ESI spectrum and in a 2011 MMT/BC spectrum (Izotov et al. 2012; Senchyna et al. 2017), suggesting that in contrast to the emission from HMXBs, the He II emission in this object is not significantly variable. In addition, in this scenario we would expect to see with equal likelihood observations of systems with enhanced $L_{X,0.5-8\text{keV}}$ due to being caught in an outburst and relatively low He II/H β (i.e. residing to the right of the models in Figure 9), which we do not observe. This argument applies also to the similar concern that geometrical beaming (as we see some evidence for in ultraluminous X-ray sources, e.g. King et al. 2001; Kaaret et al. 2017) may lead some systems to appear underluminous in X-rays while still producing strong He II; in this scenario we would also expect some systems to appear unexpectedly bright in X-rays relative to their He II emission when observed down the beam, which we do not. Even examining the larger sample of X-ray detected galaxies presented by B16, there are no instances of a measurement of an X-ray production efficiency in-excess of 10^{42} erg/s per $1 M_{\odot}$ /year SFR in any local dwarf galaxy. Thus, HMXB variability or beaming cannot readily explain the discrepancies we have discussed.

With HMXBs effectively ruled-out as the dominant source of He II in these galaxies, we consider the possibility that the model stellar ionizing spectra may simply be underestimating the flux at the He⁺-ionizing edge. Even with the latest generation of models for the expanding outer atmospheres and winds of massive stars incorporating line-blanketing and NLTE effects, the estimation of emergent flux beyond the He⁺-ionizing edge for a given star remains significantly uncertain (e.g. Gabler et al. 1992; Puls et al. 2005). In addition, there are large systematic uncertainties in predictions of the evolutionary tracks taken by stars at low metallicity, especially for those which undergo binary mass transfer. In particular, stars stripped by binary mass transfer or structurally reshaped by high rotation rates can potentially provide substantial ionizing flux beyond 54.4 eV even at relatively low initial mass (e.g. Szécsi et al. 2015; Vink 2017; Götzberg et al. 2017, 2018; Kubátová et al. 2019). Such stars have only recently been included in any form in population synthesis predictions (Eldridge & Stanway 2012; Götzberg et al. 2019), and may provide a natural explanation for both the strong metallicity dependence and lack of correlation with high specific star formation rates found for He II in dwarf galaxies (e.g. Senchyna & Stark 2019; Plat et al. 2019) as well as some of the peculiar He II nebulae lacking coincident massive stars in the Local Group (e.g. Pakull 2009; Kehrig et al. 2011). While some constraints can be placed on such stars from resolved work in the Local Group (e.g. Smith et al. 2018), extending calibrations of stellar models below the metallicity of the SMC in this way is challenging with current facilities given the limited number of appropriate resolved stellar populations (e.g. Bouret et al. 2015; Garcia et al. 2019; Evans et al. 2019). The study of nebular He II in large samples of dwarf galaxies in the context of improved stellar population synthesis models may provide some of our only insight into and constraints on such stars, which are likely to exist but challenging to directly observe.

It is still possible that other non-stellar ionizing sources

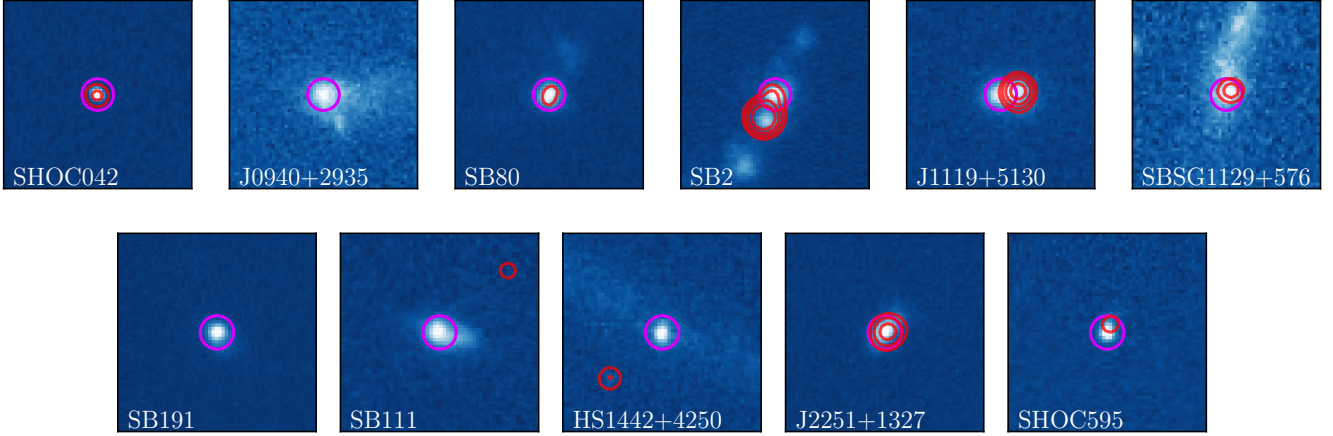


Figure 7. Optical and X-ray imaging for the eleven galaxies in our sample. The bluescale background image is a linear-scaled display of the SDSS u -band image probing light from recently-formed stars, and in red we overplot contour lines at count levels [0.25, 0.5, 1, 2] from the primary *Chandra* image after smoothing by a normalized $\sigma = 1''$ Gaussian. A purple circle with radius $2''$ centered on the optical spectral target (the brightest region in the u -band) is drawn in each case. *Chandra* X-ray sources are confidently detected within this optical radius in five cases, where it is possible for them to contribute to the observed nebular emission.

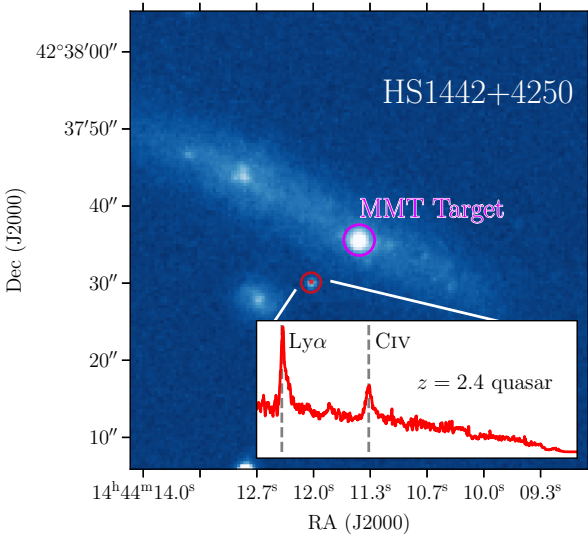


Figure 8. Follow-up spectroscopy of the X-ray source near HS1442+4250. The *Chandra* contours (red; same as Fig. 7) correspond precisely to a faint point source visible in the SDSS r -band (background bluescale image) $8''$ away from the optical star-forming region in HS1442+4250 studied with previous deep spectroscopy (outlined with a purple $2''$ -radius circle). A 10-minute MMT/BC spectrum (inset, red) reveals strong broad emission at 4130 and 5470 Å (observed-frame), which we interpret as Ly α and C IV at $z = 2.4$. In this case, the observed X-ray emission appears to be associated with a background AGN rather than an ejected HMXB associated with HS1442+4250.

contribute to the He⁺-ionizing photon budget. Fast radiative shocks driven by supernovae and stellar winds are another candidate origin for He II and Ne V emission (e.g. Dopita & Sutherland 1996; Thuan & Izotov 2005; Izotov et al. 2012; Plat et al. 2019). While galaxies with strong He II emission often lack clear signatures of significant shock-ionized gas (e.g. Senchyna et al. 2017; Kehrig et al. 2018; Berg et al.

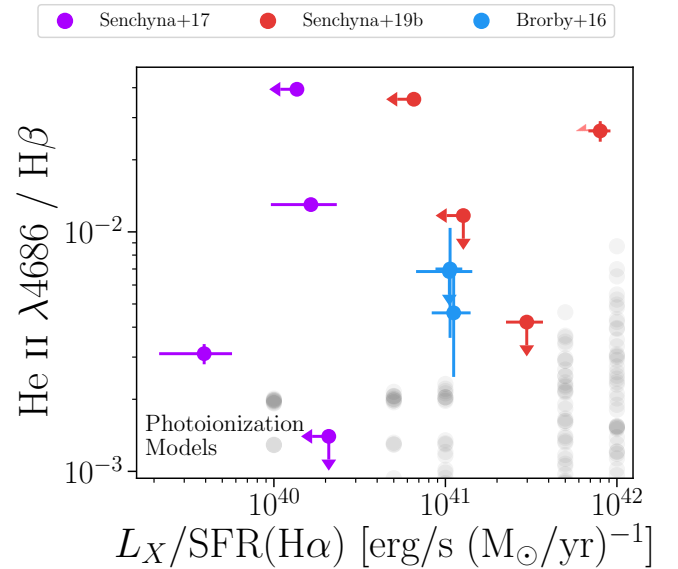


Figure 9. Observed and predicted He II/ $H\beta$ line ratios versus $L_{X,0.5-8\text{keV}}/\text{SFR}(\text{H}\alpha)$ for our observational sample and our photoionization model grid. The observed galaxies detected in He II lie uniformly in-excess of the maximal predictions of our photoionization model grid over the inferred range of X-ray production efficiencies. In addition, the most intense He II-emitters show no indication of enhanced X-ray emission relative to galaxies with less extreme He II. This comparison suggests that HMXBs are not the dominant source of He II production in this sample of galaxies.

2018), a small shock contribution can boost He II while keeping the other high-ionization UV lines consistent with observations in some cases (Plat et al. 2019). However, no predictive model of this shock contribution can yet account for the strong observed metallicity dependence in nebular He II

(though a metallicity-dependent IMF or sSFR scaling could help explain this; Plat et al. 2019). In addition, soft and supersoft X-ray sources such as accreting white dwarfs identified in the Local Group can have effective temperatures $T_{\text{eff}} \simeq 10^5\text{--}10^6$ K (corresponding to $\sim 40\text{--}400$ eV) and can potentially contribute to He⁺ ionization if they reside in a sufficiently dense ISM (e.g. Remillard et al. 1995; Di Stefano & Kong 2003, 2004; Liu et al. 2013; Woods & Gilfanov 2016; Cracco et al. 2018). Accreting intermediate-mass or supermassive black holes $> 10^3 M_{\odot}$ produce more flux at low energies than the $\leq 100 M_{\odot}$ black holes we consider here, and are potentially required to explain some of the most luminous soft X-ray sources discovered nearby (e.g. Fabbiano 2006; Kaaret et al. 2017, and references therein). Observations provide strong evidence that accreting massive black holes do reside in low-mass galaxies (e.g. Reines et al. 2013; Baldassare et al. 2015; Sartori et al. 2015) and in some cases, even in galaxies classified as star-forming by optical emission line diagnostics (Reines et al. 2020). Detailed study of many of these candidates in unresolved dwarf galaxies directly in the X-rays is challenging, however, due to their distance and relatively low luminosities (though see e.g. Baldassare et al. 2017). Deeper investigation of fainter high ionization lines like Ne v which probe photons at higher energies than 54.4 eV may provide new insight into these softer sources of EUV radiation, as well as stringently constraining their potential impact on He II.

Regardless of their impact on He II, X-ray binaries likely played a dominant role in shaping the thermal history of the very early universe. Accurate calibration of models for HMXB populations at low metallicities will prove crucial for accurate interpretation of the 21-cm signal of reionization (e.g. Furlanetto et al. 2006; Pritchard & Loeb 2010; Mesinger et al. 2013; Fragos et al. 2013b; Fialkov et al. 2014; Mirocha 2014; Mirocha & Furlanetto 2019). While much progress has been made in establishing the X-ray luminosity of low-metallicity stellar populations (Brorby et al. 2014; Douma et al. 2015; Brorby et al. 2016; Bluem et al. 2019), our results underscore the importance of expanding the sample of local galaxies with *Chandra* constraints. Of the 8 XMPs with *Chandra* detections thus far (Brorby et al. 2014), we have shown that the X-ray source in one (HS1442+4250) actually corresponds to a background quasar, and another (SB111/[RC2] A1228+12) is offset enough to make association fairly unlikely. Additional X-ray observations are needed to more confidently constrain the X-ray binary populations at the extremely low metallicities relevant for modeling the first galaxies.

5 SUMMARY

Nebular spectroscopy promises powerful insight into the physical conditions and stellar populations of galaxies, and the origin of nebular He II remains one of the most significant sources of tension in such analyses of nearby galaxies. Since the first statement of this problem (Garnett et al. 1991), HMXBs have remained a popular proposed solution. In order to assess the potential impact of HMXBs on He II and high-ionization nebular line emission more generally, we constructed a photoionization model grid using a joint SED incorporating both stellar light and a model HMXB spectrum

with variable normalization (Section 2). To test the predictions of this grid observationally, we assembled a sample of eleven $z < 0.2$ star-forming galaxies with both *Chandra* ACIS-S X-ray constraints and deep optical spectra capable of resolving nebular He II (Section 3). Our main conclusions are summarized as-follows:

(i) Due to their typically high disk temperatures, HMXBs are relatively inefficient producers of He⁺-ionizing photons even compared to typical stellar populations with a strong break at the 54.4 eV ionizing edge (Figure 1). Our photoionization modeling reveals that the low-energy tail of a HMXB spectrum can contribute significantly to He II production only for galaxies with very large X-ray luminosities for their star formation rate, exceeding 10^{42} erg/s for a $1 M_{\odot}$ /year SFR (Figure 2). Our results also indicate that if HMXBs power He II, we should find a positive correlation between He II/H β and the X-ray production efficiency $L_{X,0.5\text{--}8\text{keV}}/\text{SFR}$ among local galaxies.

(ii) Significant care must be taken in establishing physical association between X-ray emission and dwarf galaxies. We find several instances in which X-ray emission which could be associated with ejected HMXBs is nevertheless too spatially-offset from the optical regions under study spectroscopically to be physically related to the measured high-ionization emission. In addition, we find one instance in which an offset X-ray source previously identified as an HMXB actually corresponds to a background object which we identify spectroscopically as a quasar at redshift $z = 2.4$ (Figure 8).

(iii) Among our sample of nearby He II-emitters, we find X-ray production is far less efficient than we predict is required for HMXBs to power He II. In particular, our galaxies are uniformly less efficient at producing X-rays than the 10^{42} erg/s in $L_{X,0.5\text{--}8\text{keV}}$ normalized to $1 M_{\odot}$ /year lower limit that we find is required to power strong He II (i). This indicates that the HMXBs present in these systems are too faint to produce significant power at the He⁺-ionizing edge relative to the stellar SED.

(iv) We find no correlation between higher X-ray production efficiencies and stronger He II/H β in our sample. Of the three strongest He II-emitters in our sample, only one is detected in X-rays, and even in this case the X-ray emission is likely too spatially offset to be related to the observed nebular emission.

Our results suggest that HMXBs are not responsible for the nebular He II emission detected in the metal-poor galaxies in our sample. Continued observations and modeling of nebular emission from higher-ionization emission lines such as Ne v will be necessary to further constrain the potential impact of other non-stellar sources such as shocks or softer accretion systems (Section 4). However, the possibility remains that He II is indeed powered by very metal-poor stellar populations. Both stellar evolutionary and atmosphere models below the metallicity of the SMC ($Z/Z_{\odot} < 0.2$) remain entirely theoretical, and population synthesis predictions especially at the highest energies are subject to substantial systematic uncertainties. Detailed spectroscopic observations of large samples of nearby metal-poor galaxies may provide one of our best opportunities to study the physics of low-metallicity stars.

ACKNOWLEDGMENTS

The authors would like to thank Kevin Hainline and Juna Kollmeier for helpful conversations and comments. This research has made use of data obtained from the Chandra Data Archive and the Chandra Source Catalog, and software provided by the Chandra X-ray Center (CXC) in the application package CIAO. Some of the observations reported here were obtained at the MMT Observatory, a joint facility of the University of Arizona and the Smithsonian Institution. Some of the data presented herein were obtained at the W.M. Keck Observatory, which is operated as a scientific partnership among the California Institute of Technology, the University of California and the National Aeronautics and Space Administration. The Observatory was made possible by the generous financial support of the W.M. Keck Foundation. The authors wish to recognize and acknowledge the very significant cultural role and reverence that the summit of Mauna Kea has always had within the indigenous Hawaiian community. We are most fortunate to have the opportunity to conduct observations from this mountain.

D. P. S. acknowledges support from the National Science Foundation through the grant AST-1410155. J. M. acknowledges support from a CITA National Fellowship.

An allocation of computer time from the UA Research Computing High Performance Computing (HPC) at the University of Arizona is gratefully acknowledged. This research made use of ASTROPY, a community-developed core PYTHON package for Astronomy ([Astropy Collaboration et al. 2013](#)); Matplotlib ([Hunter 2007](#)); NUMPY and SCIPY ([Jones et al. 2001](#)); the SIMBAD database, operated at CDS, Strasbourg, France; and NASA's Astrophysics Data System.

REFERENCES

- Aguado D. S., et al., 2019, *ApJS*, 240, 23
- Aird J., Coil A. L., Georgakakis A., Nandra K., Barro G., Pérez-González P. G., 2015, *MNRAS*, 451, 1892
- Anders E., Grevesse N., 1989, *Geochimica Cosmochimica Acta*, 53, 197
- Astropy Collaboration et al., 2013, *A&A*, 558, A33
- Baldassare V. F., Reines A. E., Gallo E., Greene J. E., 2015, *ApJ*, 809, L14
- Baldassare V. F., Reines A. E., Gallo E., Greene J. E., 2017, *ApJ*, 836, 20
- Basu-Zych A. R., et al., 2013, *ApJ*, 774, 152
- Berg D. A., Erb D. K., Auger M. W., Pettini M., Brammer G. B., 2018, *ApJ*, 859, 164
- Berg D. A., Erb D. K., Henry R. B. C., Skillman E. D., McQuinn K. B. W., 2019a, *ApJ*, 874, 93
- Berg D. A., Chisholm J., Erb D. K., Pogge R., Henry A., Olivier G. M., 2019b, *ApJ*, 878, L3
- Bluem J., Kaaret P., Prestwich A., Brorby M., 2019, *MNRAS*, 487, 4093
- Bouret J.-C., Lanz T., Hillier D. J., Martins F., Marcolino W. L. F., Depagne E., 2015, *MNRAS*, 449, 1545
- Brinchmann J., Pettini M., Charlot S., 2008, *MNRAS*, 385, 769
- Brorby M., Kaaret P., 2017, *MNRAS*, 470, 606
- Brorby M., Kaaret P., Prestwich A., 2014, *MNRAS*, 441, 2346
- Brorby M., Kaaret P., Feng H., 2015, *MNRAS*, 448, 3374
- Brorby M., Kaaret P., Prestwich A., Mirabel I. F., 2016, *MNRAS*, 457, 4081
- Bruzual G., Charlot S., 2003, *MNRAS*, 344, 1000
- Byler N., 2018, *Nell-Byler/Cloudyfsps: Initial Release of cloudyF-SPS*, Zenodo, [doi:10.5281/zenodo.1156412](https://doi.org/10.5281/zenodo.1156412)
- Byler N., Dalcanton J. J., Conroy C., Johnson B. D., 2017, *ApJ*, 840, 44
- Cassata P., et al., 2013, *A&A*, 556, A68
- Charlot S., Longhetti M., 2001, *MNRAS*, 323, 887
- Chevallard J., Charlot S., 2016, *MNRAS*, 462, 1415
- Chisholm J., Rigby J. R., Bayliss M., Berg D. A., Dahle H., Gladsters M., Sharon K., 2019, *ApJ*, 882, 182
- Conroy C., 2013, *ARA&A*, 51, 393
- Cracco V., Orio M., Ciroi S., Gallagher J., Kotulla R., Romero-Colmenero E., 2018, *ApJ*, 862, 167
- Di Stefano R., Kong A. K. H., 2003, *ApJ*, 592, 884
- Di Stefano R., Kong A. K. H., 2004, *ApJ*, 609, 710
- Dickey J. M., Lockman F. J., 1990, *ARA&A*, 28, 215
- Dopita M. A., Sutherland R. S., 1996, *ApJS*, 102, 161
- Dopita M. A., Kewley L. J., Heisler C. A., Sutherland R. S., 2000, *ApJ*, 542, 224
- Douna V. M., Pellizza L. J., Mirabel I. F., Pedrosa S. E., 2015, *A&A*, 579, A44
- Draine B. T., 2011, *Physics of the Interstellar and Intergalactic Medium*
- Dray L. M., 2006, *MNRAS*, 370, 2079
- Eldridge J. J., Stanway E. R., 2012, *MNRAS*, 419, 479
- Eldridge J. J., Stanway E. R., Xiao L., McClelland L. A. S., Taylor G., Ng M., Greis S. M. L., Bray J. C., 2017, *Publ. Astron. Soc. Australia*, 34
- Erb D. K., Pettini M., Shapley A. E., Steidel C. C., Law D. R., Reddy N. A., 2010, *ApJ*, 719, 1168
- Evans I. N., Dopita M. A., 1985, *ApJS*, 58, 125
- Evans C. J., et al., 2019, *A&A*, 622, A129
- Fabbiano G., 2006, *ARA&A*, 44, 323
- Ferland G. J., et al., 2017, *Rev. Mex. Astron. Astrofis.*, 53, 385
- Fialkov A., Barkana R., Visbal E., 2014, *Nature*, 506, 197
- Fioc M., Rocca-Volmerange B., 2019, *A&A*, 623, A143
- Fitzpatrick E. L., 1999, *PASP*, 111, 63
- Foreman-Mackey D., Hogg D. W., Lang D., Goodman J., 2013, *PASP*, 125, 306
- Fragos T., et al., 2013a, *ApJ*, 764, 41
- Fragos T., Lehmer B. D., Naoz S., Zezas A., Basu-Zych A., 2013b, *ApJ*, 776, L31
- Fruscione A., et al., 2006, *Proc. SPIE*, 6270, 62701V
- Furlanetto S. R., Oh S. P., Briggs F. H., 2006, *Phys. Rep.*, 433, 181
- Gabler R., Gabler A., Kudritzki R. P., Puls J., Pauldrach A., 1989, *A&A*, 226, 162
- Gabler R., Gabler A., Kudritzki R. P., Mendez R. H., 1992, *A&A*, 265, 656
- García M., Herrero A., Najarro F., Camacho I., Lorenzo M., 2019, *MNRAS*, 484, 422
- Garnett D. R., Kennicutt R. C. J., Chu Y.-H., Skillman E. D., 1991, *ApJ*, 373, 458
- Gordon K. D., Clayton G. C., Misselt K. A., Landolt A. U., Wolff M. J., 2003, *ApJ*, 594, 279
- Götberg Y., de Mink S. E., Groh J. H., 2017, *A&A*, 608, A11
- Götberg Y., de Mink S. E., Groh J. H., Kupfer T., Crowther P. A., Zapartas E., Renzo M., 2018, *A&A*, 615, A78
- Götberg Y., de Mink S. E., Groh J. H., Leitherer C., Norman C., 2019, *A&A*, 629, A134
- Grimm H.-J., Gilfanov M., Sunyaev R., 2003, *MNRAS*, 339, 793
- Gutiérrez C. M., Moon D.-S., 2014, *ApJ*, 797, L7
- Gutkin J., Charlot S., Bruzual G., 2016, *MNRAS*, 462, 1757
- Heckman T. M., et al., 2005, *ApJ*, 619, L35
- Hoopes C. G., et al., 2007, *ApJS*, 173, 441
- Hummer D. G., Storey P. J., 1987, *MNRAS*, 224, 801
- Hunter J. D., 2007, *Computing In Science & Engineering*, 9, 90â&S95
- Izotov Y. I., Thuan T. X., Privon G., 2012, *MNRAS*, 427, 1229

- Jones E., Oliphant T., Peterson P., et al., 2001, SciPy: Open source scientific tools for Python
- Kaaret P., Feng H., 2013, *ApJ*, 770, 20
- Kaaret P., Alonso-Herrero A., Gallagher J. S., Fabbiano G., Zezas A., Rieke M. J., 2004a, *MNRAS*, 348, L28
- Kaaret P., Ward M. J., Zezas A., 2004b, *MNRAS*, 351, L83
- Kaaret P., Feng H., Roberts T. P., 2017, *ARA&A*, 55, 303
- Kehrig C., et al., 2011, *A&A*, 526
- Kehrig C., Vílchez J. M., Pérez-Montero E., Iglesias-Páramo J., Brinchmann J., Kunth D., Durret F., Bayo F. M., 2015, *ApJ*, 801, L28
- Kehrig C., Vílchez J. M., Guerrero M. A., Iglesias-Páramo J., Hunt L. K., Duarte-Puertas S., Ramos-Larios G., 2018, *MNRAS*, 480, 1081
- King A. R., Davies M. B., Ward M. J., Fabbiano G., Elvis M., 2001, *ApJ*, 552, L109
- Kniazev A. Y., Pustilnik S. A., Grebel E. K., Lee H., Pramskij A. G., 2004, *ApJS*, 153, 429
- Kubátová B., et al., 2019, *A&A*, 623, A8
- Lanz T., Hubeny I., 2003, *ApJS*, 146, 417
- Lebouteiller V., et al., 2017, *A&A*, 602, A45
- Leja J., Johnson B. D., Conroy C., van Dokkum P. G., Byler N., 2017, *ApJ*, 837, 170
- Levesque E. M., Leitherer C., Ekstrom S., Meynet G., Schaerer D., 2012, *ApJ*, 751, 67
- Linden T., Kalogera V., Sepinsky J. F., Prestwich A., Zezas A., Gallagher J. S., 2010, *ApJ*, 725, 1984
- Liu J.-F., Bregman J. N., Bai Y., Justham S., Crowther P., 2013, *Nature*, 503, 500
- Luridiana V., Morisset C., Shaw R. A., 2015, *A&A*, 573, A42
- Maeder A., Meynet G., 2000, *ARA&A*, 38, 143
- Mapelli M., Ripamonti E., Zampieri L., Colpi M., Bressan A., 2010, *MNRAS*, 408, 234
- McCall M. L., Rybski P. M., Shields G. A., 1985, *ApJS*, 57, 1
- Mesinger A., Ferrara A., Spiegel D. S., 2013, *MNRAS*, 431, 621
- Meurer G. R., Heckman T. M., Leitherer C., Kinney A., Robert C., Garnett D. R., 1995, *AJ*, 110, 2665
- Mineo S., Gilfanov M., Sunyaev R., 2012, *MNRAS*, 419, 2095
- Mirocha J., 2014, *MNRAS*, 443, 1211
- Mirocha J., Furlanetto S. R., 2019, *MNRAS*, 483, 1980
- Mitsuda K., et al., 1984, Publications of the Astronomical Society of Japan, 36, 741
- Nanayakkara T., et al., 2019, *A&A*, 624, A89
- Overzier R. A., et al., 2008, *ApJ*, 677, 37
- Pakull M. W., 2009, *The Magellanic System: Stars, Gas, and Galaxies*, 256, 437
- Pakull M. W., Angebault L. P., 1986, *Nature*, 322, 511
- Pauldrach A. W. A., Hoffmann T. L., Lennon M., 2001, *A&A*, 375, 161
- Plat A., Charlot S., Bruzual G., Feltre A., Vidal-García A., Morisset C., Chevallard J., Todt H., 2019, arXiv e-prints, p. arXiv:1909.07386
- Prestwich A. H., Tsantaki M., Zezas A., Jackson F., Roberts T. P., Foltz R., Linden T., Kalogera V., 2013, *ApJ*, 769, 92
- Pritchard J. R., Loeb A., 2010, *Phys. Rev. D*, 82, 023006
- Puls J., Urbaneja M. A., Venero R., Repolust T., Springmann U., Jokuthy A., Mokiem M. R., 2005, *A&A*, 435, 669
- Reines A. E., Greene J. E., Geha M., 2013, *ApJ*, 775, 116
- Reines A. E., Condon J. J., Darling J., Greene J. E., 2020, *ApJ*, 888, 36
- Remillard R. A., Rappaport S., Macri L. M., 1995, *ApJ*, 439, 646
- Salpeter E. E., 1955, *ApJ*, 121, 161
- Sanders R. L., et al., 2016, *ApJ*, 816, 23
- Sartori L. F., Schawinski K., Treister E., Trakhtenbrot B., Koss M., Shirazi M., Oh K., 2015, *MNRAS*, 454, 3722
- Schaerer D., Fragas T., Izotov Y. I., 2019, *A&A*, 622, L10
- Schlafly E. F., Finkbeiner D. P., 2011, *ApJ*, 737, 103
- Senchyna P., Stark D. P., 2019, *MNRAS*, 484, 1270
- Senchyna P., et al., 2017, *MNRAS*, 472, 2608
- Senchyna P., Stark D. P., Chevallard J., Charlot S., Jones T., Vidal-García A., 2019, *MNRAS*, 488, 3492
- Sheinis A. I., Bolte M., Epps H. W., Kibrick R. I., Miller J. S., Radovan M. V., Bigelow B. C., Sutin B. M., 2002, *PASP*, 114, 851
- Shirazi M., Brinchmann J., 2012, *MNRAS*, 421, 1043
- Shirazi M., Brinchmann J., Rahmati A., 2014, *ApJ*, 787, 120
- Smith N., Götberg Y., de Mink S. E., 2018, *MNRAS*, 475, 772
- Stanway E. R., Eldridge J. J., 2018, *MNRAS*, 479, 75
- Stanway E. R., Eldridge J. J., 2019, *A&A*, 621, A105
- Stanway E. R., Eldridge J. J., Becker G. D., 2016, *MNRAS*, 456, 485
- Steidel C. C., Strom A. L., Pettini M., Rudie G. C., Reddy N. A., Trainor R. F., 2016, *ApJ*, 826, 159
- Stoll R., Prieto J. L., Stanek K. Z., Pogge R. W., Szczygiel D. M., Pojmański G., Antognini J., Yan H., 2011, *ApJ*, 730, 34
- Swartz D. A., Soria R., Tennant A. F., Yukita M., 2011, *ApJ*, 741, 49
- Szécsi D., Langer N., Yoon S.-C., Sanyal D., de Mink S., Evans C. J., Dermine T., 2015, *A&A*, 581, A15
- Thuan T. X., Izotov Y. I., 2005, *ApJS*, 161, 240
- Thuan T. X., Bauer F. E., Papaderos P., Izotov Y. I., 2004, *ApJ*, 606, 213
- Tonry J. L., Blakeslee J. P., Ajhar E. A., Dressler A., 2000, *ApJ*, 530, 625
- Vázquez G. A., Leitherer C., Schaerer D., Meynet G., Maeder A., 2007, *ApJ*, 663, 995
- Vink J. S., 2017, *A&A*, 607, L8
- Woods T. E., Gilfanov M., 2016, *MNRAS*, 455, 1770
- Zuo Z.-Y., Li X.-D., 2010, *MNRAS*, 405, 2768

APPENDIX A: GALAXY-BY-GALAXY ANALYSIS

Correctly interpreting both high-ionization nebular emission lines and X-ray imaging constraints requires careful analysis on an individual galaxy basis. Here, we outline and discuss the observational results obtained for each galaxy in our sample and our synthesis of the X-ray and optical data. Where available, we compare to previously-published X-ray luminosities derived from the same datasets by [Brorby et al. \(2014, 2016\)](#).

SHOC 042 (spectroscopically characterized in the SDSS H II galaxies with Oxygen abundances Catalog, SHOC; [Kniazev et al. 2004](#)) is a compact star-forming galaxy at $z = 0.167$ classified as an LBA on the basis of high FUV luminosity and surface brightness comparable to LBGs at high redshift ([Heckman et al. 2005](#); [Hoopes et al. 2007](#); [Overzier et al. 2008](#)). It is the most distant galaxy in our sample at 805 Mpc, hosts relatively high metallicity gas at $12 + \log O/H = 8.21$, and harbors the largest star formation rate in our sample: $SFR(H\alpha) = 5.9 M_{\odot}/\text{yr}$ (Section 3.2). Nebular He II is detected in this system with MMT/BC (Figure 6), with $He II/H\beta = 0.0046 \pm 0.0021$. In the *Chandra* ACIS-S image of this source (ObsID: 16019, PI: Kaaret), we detect a source $0.2''$ (0.7 comoving kpc) away from the center of the optical spectroscopic target (within our adopted 99% confidence spatial offset tolerance of $1.4''$: Section 3.4), with a derived luminosity in the 0.5–8 keV band of $6.6 \pm 1.6 \times 10^{41}$ erg/s (Table 4). This flux measurement is in agreement (within 1.5σ) with that of [Brorby et al. \(2016\)](#)

using the same dataset ⁴. This corresponds to an X-ray production efficiency of $1.1 \pm 0.3 \times 10^{41}$ erg/s per M_{\odot} /year of star formation.

J0940+2935 (KUG 0937+298 in Brorby et al. 2014) is a tadpole-shaped dwarf galaxy at $z = 0.0024$ (8 Mpc), the most nearby galaxy in our sample (S19). This system is two orders of magnitude closer and presents an SFR more than four orders of magnitude lower than SHOC 042 ($10^{-3.6} M_{\odot}$ /year), and harbors gas with an oxygen abundance clearly in the XMP regime ($12 + \log O/H = 7.63 \pm 0.14$). The Keck/ESI spectrum of this source reveals no nebular He II ($He II/H\beta < 1.2 \times 10^{-2}$), and the 5 ks *Chandra* exposure (ObsID: 11301, PI: Prestwich) reveals no significant detections within an arcminute of the galaxy (2.3 comoving kpc), in agreement with Brorby et al. (2014). Our 95% confidence upper limit places this galaxy at an X-ray production efficiency of $< 1.3 \times 10^{41}$ erg/s per M_{\odot} /year.

SB 80 is a bright star-forming region embedded in UGC 5189 at 46 Mpc distance, and hosts moderately metal-poor gas at $12 + \log O/H = 8.24 \pm 0.06$ (S17). Our deep Keck/ESI spectrum reveals both a broad stellar and a clearly-differentiated nebular component to He II, with the narrow component measured at $He II/H\beta = 0.0031 \pm 0.0003$. This system was observed in seven different *Chandra* pointings targeting the luminous supernova 2010jl (positioned $1.7''$ away from the star-forming region under study; Stoll et al. 2011) from 2010–2018. The longest and most recent of these observations (ObsID: 19164; 46.8 ks, taken 2018-01-03) reveals a source at $0.2''$ measured separation from the optical target, with $L_{X,0.5-8\text{keV}} = 4.9 \pm 2.2 \times 10^{38}$ erg/s ($2.0^{+0.9}_{-0.8} \times 10^{-15}$ erg/s/cm²). The exposure times and target positions on-chip for the other six observations vary significantly, with some indication of lower flux at the $\sim 2\sigma$ level in one observation but no statistically-significant differences in the other cases ⁵. For this work, we proceed with the highest-confidence flux measurement obtained in ObsID: 19164, which is also the highest measured flux for this source. At a star formation rate of $0.13 M_{\odot}$ /year, the measured X-ray luminosity (Table 4) corresponds to $3.9 \pm 1.8 \times 10^{39}$ erg/s in the 0.5–8 keV band per M_{\odot} /year of star formation.

SB 2 is a dwarf galaxy at a distance of 19 Mpc dominated by four star-forming clumps. SDSS and Keck/ESI spectroscopy of the brightest of these clumps reveals prominent nebular emission in the He II $\lambda 4686 \text{ \AA}$ line, with $He II/H\beta = 0.0130 \pm 0.0006$ (S17) and a star formation rate from the Balmer lines of $10^{-1.61} M_{\odot}$ /year. This sys-

tem was observed with a 15 ks *Chandra* observation (ObsID: 19463, PI: Mezcua, not yet published), revealing an X-ray source coincident with the optical clump observed with ESI ($r_{\text{sep}} = 0.3''$) with a computed luminosity of $L_{X,0.5-8\text{keV}} = 4.0 \pm 1.7 \times 10^{38}$ erg/s. The optical clump to the southeast of the spectroscopically-targeted region also has an associated X-ray detection, with an even higher luminosity $L_{X,0.5-8\text{keV}} = 5.3 \pm 0.5 \times 10^{39}$ erg/s; but since this second source is $3.2''$ away, we conclude it cannot contribute to the observed nebular flux and ignore it in this analysis. This X-ray luminosity corresponds to a production efficiency of $1.6 \pm 0.7 \times 10^{40}$ erg/s per unit M_{\odot} /year.

J1119+5130 ([RC2] A1116+51 in Brorby et al. 2014) is a compact XMP ($12 + \log O/H = 7.51 \pm 0.07$) at 22 Mpc forming stars at $SFR(H\alpha) = 10^{-2.3} M_{\odot}$ /year (S19). This galaxy shows strong nebular He II in a Keck/ESI spectrum at $He II/H\beta = 0.026 \pm 0.003$ (S19). We detect an X-ray source in the 11.7 ks *Chandra* exposure covering this galaxy (ObsID: 11287, PI: Prestwich), with a luminosity of $L_{X,0.5-8\text{keV}} = 3.9 \pm 0.4 \times 10^{39}$ erg/s in good agreement with that reported in Brorby et al. (2014, after correcting for the small difference in adopted distances; 22 versus 20.8 Mpc). However, we find this source to be offset by $2.2''$ from the center of the star-forming region we target, which is larger than the expected astrometric uncertainties of the ACIS-S data (Section 3.4). This places the X-ray source outside of the $1''$ slit and extraction box used with Keck/ESI, and corresponds to 0.2 kpc at the distance of this galaxy. However, it overlaps the other side of this compact galaxy in the optical (Figure 7). Thus, while it is unlikely that this X-ray source contributes to the nebular He II observed in the Keck/ESI spectrum, it does appear to be clearly associated with the galaxy. We consider this galaxy detected with *Chandra*, but note this caveat in Table 4 and in Figure 9. This detection yields an X-ray production efficiency of $8.0 \pm 1.2 \times 10^{41}$ erg/s for a star formation rate of $1 M_{\odot}$ /year, the highest of our sample. If we instead adopt the 95% confidence upper limit on the X-ray flux obtained by applying SRCFLUX to the *Chandra* image at the precise coordinates of the ESI target, the X-ray production efficiency is constrained to $< 2.2 \times 10^{40}$ erg/s per M_{\odot} /year, over an order of magnitude lower.

SBGS1129+576 is a tadpole-like XMP at 25 Mpc dominated by a star-forming clump targeted with SDSS and Keck/ESI spectroscopy (S19). These spectra reveal a very low oxygen abundance $12 + \log O/H = 7.47 \pm 0.06$ and an SFR of $10^{-2.5} M_{\odot}$ /year, but a nondetection of nebular He II, $He II/H\beta < 0.004$ (low signal-to-noise positive flux is visible at He II in the Keck/ESI spectrum, but with FWHM significantly larger than the strong nebular lines, so we conclude it is stellar in origin: S19). An X-ray source is also detected in this galaxy with *Chandra* (ObsID: 11283, PI: Prestwich), at a luminosity of $L_{X,0.5-8\text{keV}} = 11 \pm 2 \times 10^{38}$ erg/s and at $0.8''$ separation from the center of the clump observed with ESI (within our adopted offset tolerance). This source was also identified by Brorby et al. (2014) at a luminosity in good agreement with our measurement. This measurement yields an X-ray production efficiency of $3.0 \pm 0.7 \times 10^{41}$ erg/s per M_{\odot} /year.

SB191 (S17) is a compact star-forming H II-region embedded in the large spiral galaxy NGC 4204 at 10 Mpc distance, and hosts gas at a moderate oxygen abundance of $12 + \log O/H = 8.30 \pm 0.07$ with star formation rate $10^{-2.2}$

⁴ Since Brorby et al. 2016 extract flux in a large predefined ellipse rather than using SRCFLUX, small offsets such as this are expected.

⁵ Three other observations covering SB 80 with exposure times ~ 40 ks exist: 13781 (40.51 ks; PI: Chandra, 2011-10-17), 13782 (39.54 ks; PI: Chandra, 2012-06-10), and 15869 (39.54 ks; PI: Chandra, 2014-06-01). A coincident source is detected in 13781, with lower flux by a factor of ten at 2σ significance ($3.2^{+4.5}_{-2.9} \times 10^{-16}$ erg/s/cm²); 13782 also shows a detection, with flux consistent with 19164 ($1.8^{+0.8}_{-0.7} \times 10^{-15}$ erg/s/cm²); and in 15869, no source is detected within $20''$, but the $1 - \sigma$ flux distribution measured in 19164 is not excluded by the 90% confidence upper limit. Likewise, no spatially-consistent source is detected in the remaining three observations with exposure times ranging from 10–20 ks, (11122 PI: Chandra, 11237 PI: Pooley, 13199 PI: Chandra), but the 90% confidence limits are all $\geq 2.3 \times 10^{-15}$ erg/s/cm².

M_{\odot}/year . This system is undetected in nebular He II, with a purely broad stellar component identified with Keck/ESI. The host galaxy NGC 4204 was observed with *Chandra*/ACIS-S in a single 2 ks pointing (ObsID: 7092, PI: Swartz) targeting a ULX candidate in another part of the galaxy (Swartz et al. 2011). The star-forming region we have targeted is more than an arcminute away from the ULX candidate studied in this previous analysis, but still near enough to the center of the S3 chip for confident source detection. This short exposure reveals no X-ray target detections within $45''$ (> 2 comoving kpc) of SB191, placing a 95% upper limit on the X-ray luminosity of $L_{X,0.5-8\text{keV}} < 1.3 \times 10^{38}$ erg/s (corresponding to $< 2.1 \times 10^{40}$ erg/s per M_{\odot}/year).

SB111 ([RC2] A1228+12 in Brorby et al. 2014) is a blue compact dwarf at 16 Mpc, with low-metallicity gas at $12 + \log \text{O}/\text{H} = 7.81 \pm 0.08$ just above the XMP cutoff and a star formation rate from the Balmer lines of $10^{-2.4} M_{\odot}/\text{year}$ (S17). This system has one of the strongest nebular He II lines detected among local star-forming galaxies, with $\text{He II}/\text{H}\beta = 0.039 \pm 0.001$ measured with Keck/ESI. In addition, a deep MMT/BC spectrum was obtained for this target by Izotov et al. (2012). This spectrum revealed both He II (with $\text{He II}/\text{H}\beta = 0.038 \pm 0.002$ in very good agreement with our later Keck/ESI measurement) and a 2σ detection of Ne v $\lambda 3426$, with $\text{Ne v}/\text{H}\beta = 0.79 \pm 0.36$ (Table 3). SB 111 was also targeted with *Chandra* (ObsID: 11290, PI: Prestwich), and an associated X-ray detection with $L_{X,0.5-8\text{keV}} = 3.4 \times 10^{38}$ erg/s was reported by subsequent analyses (Prestwich et al. 2013; Brorby et al. 2014; Douma et al. 2015). However, as noted in S17 and confirmed by the reanalysis presented in this work, this X-ray source is offset from the optical galaxy by $11.1''$ (or 0.9 kpc comoving kpc; Figure 7). While it is possible this is an ejected HMXB associated with star formation in this galaxy, this X-ray source cannot in any case contribute to excitation of the observed nebular He II. For the purposes of this work, then, SB111 is undetected in X-rays, with $L_{X,0.5-8\text{keV}} < 0.6 \times 10^{38}$ erg/s ($< 1.4 \times 10^{40}$ erg/s per M_{\odot}/year).

HS1442+4250 is a somewhat more extended XMP ($12 + \log \text{O}/\text{H} = 7.65 \pm 0.04$) which hosts a compact star-forming region with $\text{SFR}(\text{H}\alpha) = 10^{-3.0} M_{\odot}/\text{year}$ that we observed with MMT and Keck spectroscopy in S19. The Keck spectroscopy reveals He II at a similar intensity to that found in SB111, with $\text{He II}/\text{H}\beta = 0.0358 \pm 0.0006$, among the highest observed. This galaxy was also in the sample studied with *Chandra* in Brorby et al. (2014), where an X-ray source was reported with luminosity $L_{X,0.5-8\text{keV}} = 2.2 \times 10^{38}$ erg/s (ObsID: 11296, PI: Prestwich). Our *Chandra* reanalysis revealed that as in the case of SB111, this X-ray source was significantly offset from the optical galaxy, at a distance of $8.3''$ (corresponding to 0.4 comoving kpc) where contribution to the optical nebular line flux is impossible. In this case, we noted that the observed X-ray source was coincident with a faint point source in the SDSS image (at 14h44m12.01s, +42d37m30.05s; $g = 25.1$, $i = 21.03$). On the night of April 15 2018, we observed this target with MMT/BC for 10 minutes. The extracted spectrum revealed strong broad asymmetric emission at 4130 and 5270 Å, which we interpret as Ly α and C IV $\lambda 1548, 1550$ at redshift $z = 2.4$. At this redshift, the observed flux corresponds to a rest-frame $\sim 2-27$ keV band luminosity of 1.3×10^{45} erg/s, just above the knee of the observed AGN luminosity function at $z \sim 2$ (Aird et al. 2015).

Thus in this case, the X-ray emission previously identified as associated with this galaxy appears to originate entirely from a distant quasar in chance projection rather than an ejected HMXB. We place an upper limit on X-ray flux from the optical target of $L_{X,0.5-8\text{keV}} < 0.6 \times 10^{38}$ erg/s (corresponding to a production efficiency of $< 6.6 \times 10^{40}$ erg/s per M_{\odot}/year).

J2251+1327 is a relatively distant (279 Mpc) LBA described in Brorby et al. (2016) with direct- T_e gas-phase metallicity $12 + \log \text{O}/\text{H} = 8.29 \pm 0.06$ and $\text{SFR}(\text{H}\alpha) = 1.7 M_{\odot}/\text{year}$. Our MMT/BC spectrum yields a detection of nebular He II, with modestly large $\text{He II}/\text{H}\beta = 0.0070 \pm 0.0034$; but no Ne v ($\text{Ne v}/\text{H}\beta < 0.62$). We find a clear X-ray detection in the *Chandra* ACIS-S image of this galaxy (ObsID: 13013, PI: Basu-Zych) separated by $0.4''$ from the center of the optical target (0.5 comoving kpc, but within our spatial offset tolerance of $1.4''$), with luminosity $L_{X,0.5-8\text{keV}} = 1.77 \pm 0.30 \times 10^{41}$ erg/s consistent with the measurement of Brorby et al. (2016). This results in an estimate of the X-ray production efficiency of $1.1 \pm 0.2 \times 10^{41}$ erg/s per M_{\odot}/year .

SHOC 595 is another LBA at similarly large distance (589 Mpc) hosting the highest-metallicity gas in our sample along with SB191 ($12 + \log \text{O}/\text{H} = 8.30 \pm 0.14$). The He II profile measured with MMT/BC for this galaxy is broader than the other nebular lines (Section 3.3), and we fail to detect a clear narrow contribution at 2σ ($\text{He II}/\text{H}\beta < 0.68$) or Ne v ($\text{Ne v}/\text{H}\beta < 0.62$). We detect a luminous X-ray source in the 13.6 ks *Chandra* observation (ObsID: 17418, PI: Kaaret), with luminosity $3.2 \pm 1.1 \times 10^{41}$ erg/s, 1σ lower than the measurement presented by Brorby et al. (2016). The source is offset by $1.3''$ from the optical center of the galaxy, which corresponds to a large physical distance of 3.6 comoving kpc but is within our adopted r_{sep} cutoff representing the 99% confidence interval of the *Chandra* positional accuracy (Section 3.4). This galaxy was observed in 2 separate instances, but the system was not detected in the other 9.1 ks integration (ObsID: 16020), with a 90% confidence limiting flux just below that measured in 17418. We adopt the former flux measurement, yielding an X-ray production efficiency of $1.1 \pm 0.4 \times 10^{41}$ erg/s per M_{\odot}/year , and discuss the impact of this possible variability in Section 4.